Geological Magazine

www.cambridge.org/geo

Characteristics and application of present *in situ* stress field of a strike-slip fault: a 3D finite-element simulation study

Teng Zhao[1,2,*], Jibiao Zhang[2,*], Wenlong Ding[1], Rui Zhao[2], Ahmed E Radwan[3] and Xinghua Wang[2]

[1]School of Energy Resource, China University of Geosciences, Beijing 100083, China; [2]Petroleum Exploration and Production Research Institute, SINOPEC, Beijing, 100083, China and [3]Institute of Geological Sciences, Faculty of Geography and Geology, Jagiellonian University, Gronostajowa 3a, 30-387, Cracow, Poland

Original Article

Cite this article: Zhao T, Zhang J, Ding W, Zhao R, Radwan AE, and Wang X (2023) Characteristics and application of present *in situ* stress field of a strike-slip fault: a 3D finite-element simulation study. *Geological Magazine* **159**: 2361–2378. https://doi.org/10.1017/S0016756822000942

Received: 6 January 2022
Revised: 31 July 2022
Accepted: 27 August 2022
First published online: 19 October 2022

Keywords:
strike-slip fault; finite-element simulation; present *in situ* stress; fracture; Tarim Basin

Authors for correspondence:
Wenlong Ding, Ahmed E. Radwan
Emails: dingwenlong2006@126.com; radwanae@yahoo.com; ahmed.radwan@uj.edu.pl

*Teng Zhao and Jibiao Zhang contributed equally to this work, and they are co-first authors.

Abstract

Previous hydrocarbon explorations in the middle of the Tarim Basin indicate that strike-slip faults play an important role in the development of Ordovician carbonate reservoirs and hydrocarbon accumulation. The SB5 fault in the Tarim Basin was the target of this investigation. An evaluation of the stress *in situ* was carried out and provided boundary conditions to build a 3D geomechanical model. The distribution and application of present *in situ* stress in the strike-slip fault were studied. The results show good agreement between the absolute measured stress *in situ* and the modelled stresses, revealing a different stress regime along the strike-slip fault. The uplift segment belongs to a strike-slip stress state, and other areas belong to a normal fault stress state. The strike-slip fault has a significant influence on the present *in situ* stress distribution. The direction of the maximum horizontal stress deflects near the fault and tends to be parallel to the fault strike. This work introduces a comprehensive evaluation of the present *in situ* stress of the fractured carbonate reservoirs controlled by the strike-slip fault system. The present *in situ* stress direction can clarify the propagation direction of hydraulic fracturing and serve to evaluate the effectiveness of natural fractures.

Introduction

Previous hydrocarbon exploration experiences in the central Tarim Basin have indicated that the fractured–vuggy carbonate reservoirs develop along strike-slip faults (Yu *et al.* 2016; Lu *et al.* 2017). The major breakthrough of the Northwest Oilfield Branch Company (SINOPEC) in the T-SH oilfield has further indicated that strike-slip faults play an important role in the development of Ordovician carbonate fractured reservoirs for oil and gas accumulation (Qi, 2016; Jiao, 2017). The reservoir type in the middle of the Tarim Basin is a fault-controlled carbonate reservoir (Song *et al.* 2013; Zhao *et al.* 2019). Previous studies mainly focused on the geometric (Deng *et al.* 2018, 2019; Wang *et al.* 2020) and kinematic characteristics of strike-slip faults in the central Tarim Basin (Han *et al.* 2017). However, little effort has been made regarding the present *in situ* stress distribution of the strike-slip fault system. Research on the distribution and application of present *in situ* stress has important guiding significance for petroleum engineering design, reservoir reconstruction and hydraulic fracturing (Gale *et al.* 2007; Engelder *et al.* 2009; Radwan *et al.* 2021).

The present *in situ* stress field is affected by topography, lithology, structure, mechanical properties, fluid pressure and other factors (Nenna & Aydin, 2011; Radwan & Sen, 2021*a*, *b*). How to accurately obtain the present *in situ* stress field has always been a challenging problem for petroleum engineering (Hopkins, 1997). The study of present *in situ* stress is usually carried out through *in situ* measurement and stress modelling (either analytical or numerical); *in situ* stress measurement is usually carried out through logging data, acid fracturing curve and rock experiment (Djurhuus & Aadnoy, 2003; Cui and Radwan, 2022; Xie *et al.* 2022), while stress modelling (either analytical or numerical) includes the finite-element method (Hampel & Hetzel, 2015; Khodaverdian *et al.* 2015), the boundary element method (T Zhao *et al.* 2021) and the discrete element method (Qu *et al.* 2011). The finite-element method is widely used in numerical simulations of the present *in situ* stress, due to its accurate quantitative and discrete approximation, and it is a key method for oil and gas exploration and development and fault formation mechanism identification (Bertoluzza & Perotti, 1997; Candela *et al.* 2015; Gao, 2021). The distribution of the present *in situ* stress field can be applied to fracture prediction (Pollard & Segall, 1987; Zoback, 2007; Zhang *et al.* 2018; Maerten *et al.* 2019), reservoir 'sweet spot' prediction (Zhou *et al.* 2012) and mud window determination (Mousavipour *et al.* 2020).

The SB5 fault is the main dividing line of E–W zoning of the strike-slip fault system in the Tarim Basin. The fault strike in the west is mainly NW-trending, and the fault strike in the east is

mainly NE-trending. The SB5 fault is an important target of oil and gas exploration at present, with full coverage of 3D seismic data. In this study, the SB5 fault was taken as the research object, and the geological model was established based on the interpretation results of 3D seismic data. The results of the regional present *in situ* stress magnitude and direction were taken as boundary conditions, and collected rock physical test reports provided model rock mechanical parameters. A 3D geomechanical model is implemented to better understand the control of faults and structures on the stress field. *In situ* stress analysed by the finite-element method, and stress measured *in situ* were used to calibrate the model. Based on the *in situ* stress distribution, the propagation direction of hydraulic fractures and effectiveness evaluation of natural fractures were studied.

Geological setting

The T-SH area is located in the north of the Shuntuoguole Low Uplift, a secondary structural unit located in the Tarim Basin, the largest intracratonic basin in China. The study area encompasses the Kataka Uplift to the north, the Shaya Uplift to the south, the Manjiaer Depression to the east and the Awati Depression to the west (Fig. 1). The T-SH area of the Tarim Basin is an Ordovician ultra-deep fault-controlled carbonate oilfield. Oil and gas resources are mainly contained in the marine carbonate formation of the middle and lower Ordovician in the platform basin. The target formation in the T-SH area is Ordovician carbonate rock of the Yijianfang Formation (Fig. 2). The thickness of the Yijianfang Formation is *c.* 160 m.

The research objects of this paper are in the northern section of the SB5 fault. The SB5 fault is characterized by plane segmentation and vertical stratification (Jiao, 2018). It is N-NW-trending in the Shun 8 North 3D work area, which is divided into ten segments. These are mostly arranged in a left-stepping configuration, and overlapped areas are developed between the segments (Fig. 3b–d). It is inferred that the SB5 fault is dextral strike-slip at the T_7^4 interface (top of the Ordovician Yijianfang Formation), and the left-stepping en echelon normal fault developed at the T_7^0 interface (top of Ordovician Sangtamu Formation) is also dextral strike-slip (Deng *et al.* 2019). In the formation period, the translation segment formed under a single regional strike-slip event. The two strike-slip faults overlap in the step area and are in a state of tension torsion or compression torsion (Mcclay & Bonora, 2001; Woodcock & Rickards, 2003). The overlapping areas can be divided into pull-apart segments and uplift segments. The pull-apart segment is characterized by an extensional component, forming normal faults, extensional strike-slip dual structure and pull-apart basins. The uplift section is characterized by a compressive component, forming reverse faults, fold and uplift (Alsop, 2009). There are three deformation styles distributed along ten segments dividing up the northern section of the SB5 fault (Deng *et al.* 2019).

Data and methodology

Seven wells (S1–S7) were selected in the SB1, SB5 and SB7 faults, including log data, geological reports and core samples. The well-log datasets are wireline logs of gamma-ray, density, resistivity and sonic curves, and formation micro-imager (FMI) logs that were used for *in situ* stress analysis based on observed drilling-induced fractures and borehole breakout. The core samples are used for mechanical experiments to determine the rock mechanical parameters and *in situ* stress. When establishing the 3D geomechanical model, we focus on the influence of strike-slip faults on the stress field. The research workflow diagram is shown in Fig. 4. Firstly, the SB5 fault was interpreted according to the 3D seismic data, and the geological model was established. Secondly, the rock mechanical parameters were calculated using logging data, and different mechanical parameters were given to different layers and structural parts of the geological model (Table 1). The present *in situ* stress magnitude and direction of a single well were obtained by comprehensive use of logging data and rock mechanics experiment as the boundary conditions for model loading. Finally, based on the established geological mechanical model, the finite-element method was used to carry out the numerical simulation of the stress field, establish a three-dimensional *in situ* stress distribution model and verify it with the calculation results of a single well. The distribution of the present *in situ* stress of SB5 was clarified, providing a basis for the study of the fracture propagation law of hydraulic fracturing and the optimization of the targeted acid fracturing process.

Fault description based on seismic data

High-quality 3-D seismic volumes collected by SINOPEC cover the SB5, SB1 and SB7 faults. The seismic dataset used here has a bin spacing of 25 × 25 m with a main frequency of 30–40 Hz, which are favourable parameters for detailed structural mapping and seismic reservoir description. The processed seismic data (time-migrated) were used for interpretation. The seismic coherence technique was used to image fault-induced discontinuities (Bahorich & Farmer, 1995).

Rock mechanics parameters

Young's modulus and Poisson's ratio are elastic mechanical properties. In this study, the rock mechanical parameters were obtained through triaxial mechanical experiments.

The maximum confining pressure of a triaxial rock mechanics tester is 100 MPa, the maximum simulated well depth is 10 000 m and the system accuracy error is less than 0.0005 %. The simulated formations are ultra-deep (>6000 m). Due to the deep buried depth (about 7000 m), the real geological conditions are inaccessible, hence, only the experimental conditions with the highest temperature and pressure can be selected. The ones with confining pressure of 60 MPa and temperature of 140 °C were selected.

Present *in situ* stress magnitude

The distribution of present *in situ* stress is mainly reflected in its direction and magnitude. For a strike-slip fault, reliable *in situ* stress results can be obtained only by using a variety of effective methods. In this paper, the acoustic emission (AE) experiment and logging evaluation method were used to determine the *in situ* stress magnitude of the target layer.

Acoustic emission (AE) experiment

The principle of the AE experiment is based on the Kaiser effect. The Kaiser effect means that the internal strain energy of rock will be released quickly after deformation. When the stress reaches the maximum stress in history, the elastic wave release phenomenon will be very obvious (Kaiser. 1950). Kanagawa *et al.* (1977) first applied this method to the calculation of *in situ* stress. The present *in situ* stress results obtained by other methods can be used as the basis for calibration points (Lan *et al.* 2021). A Triaxial Rock mechanics tester is used for loading, and a rock acoustic emission high-performance analyser is used to monitor the Kaiser point. Experiments were carried out under conditions of confining pressure 20 MPa, pore pressure 0 MPa and room temperature.

https://doi.org/10.1017/S0016756822000942 Published online by Cambridge University Press

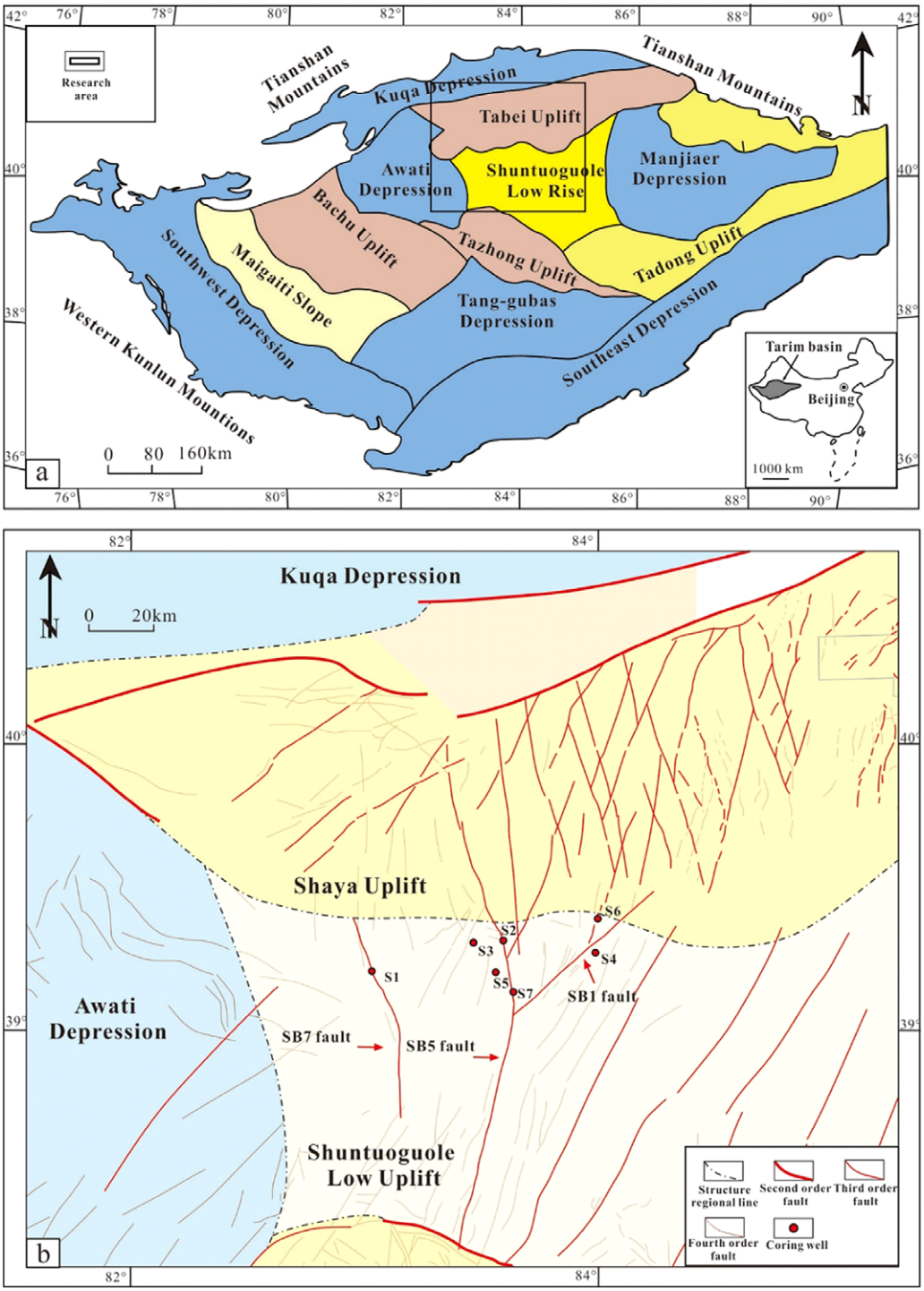

Fig. 1. (a) Simplified distribution map of the tectonic units in the Tarim Basin. (b) Detail of the strike-slip fault distribution at the top of the Middle–Upper Ordovician (interface T_7^4) in the north of the Shuntuoguole Low Uplift.

According to the measured Kaiser effect point stress, the principal stress is calculated as follows:

$$\begin{aligned} &\sigma_v + \sigma_\perp + \alpha p_p - p_c \\ \sigma_H &= \frac{\sigma_0+\sigma_{90}}{2} + \frac{\sigma_0-\sigma_{90}}{2}(1+\tan^2 2\theta)^{\frac{1}{2}} + \alpha p_p - p_c \\ \sigma_h &= \frac{\sigma_0+\sigma_{90}}{2} + \frac{\sigma_0-\sigma_{90}}{2}(1+\tan^2 2\theta)^{\frac{1}{2}} + \alpha p_p - p_c \\ \tan 2\theta &= \frac{\sigma_0+\sigma_{90}-2\sigma_{45}}{\sigma_0-\sigma_{90}} \end{aligned} \quad (1)$$

where $\sigma_\perp$ (MPa) is the Kaiser point stress of the vertical coring rock sample, σ_0 (MPa) is the Kaiser point stress of 0° coring rock sample, σ_{45} (MPa) is the Kaiser point stress of 45° coring rock sample, σ_{90} (MPa) is the Kaiser point stress of 90° coring rock sample, Pp (MPa) is the pore pressure, P_C (MPa) is the confining pressure and α is the effective stress coefficient.

Logging evaluation

The vertical principal stress is determined by the gravitational gradient of the overlying strata and can be obtained by integrating the density logging curve using

https://doi.org/10.1017/S0016756822000942 Published online by Cambridge University Press

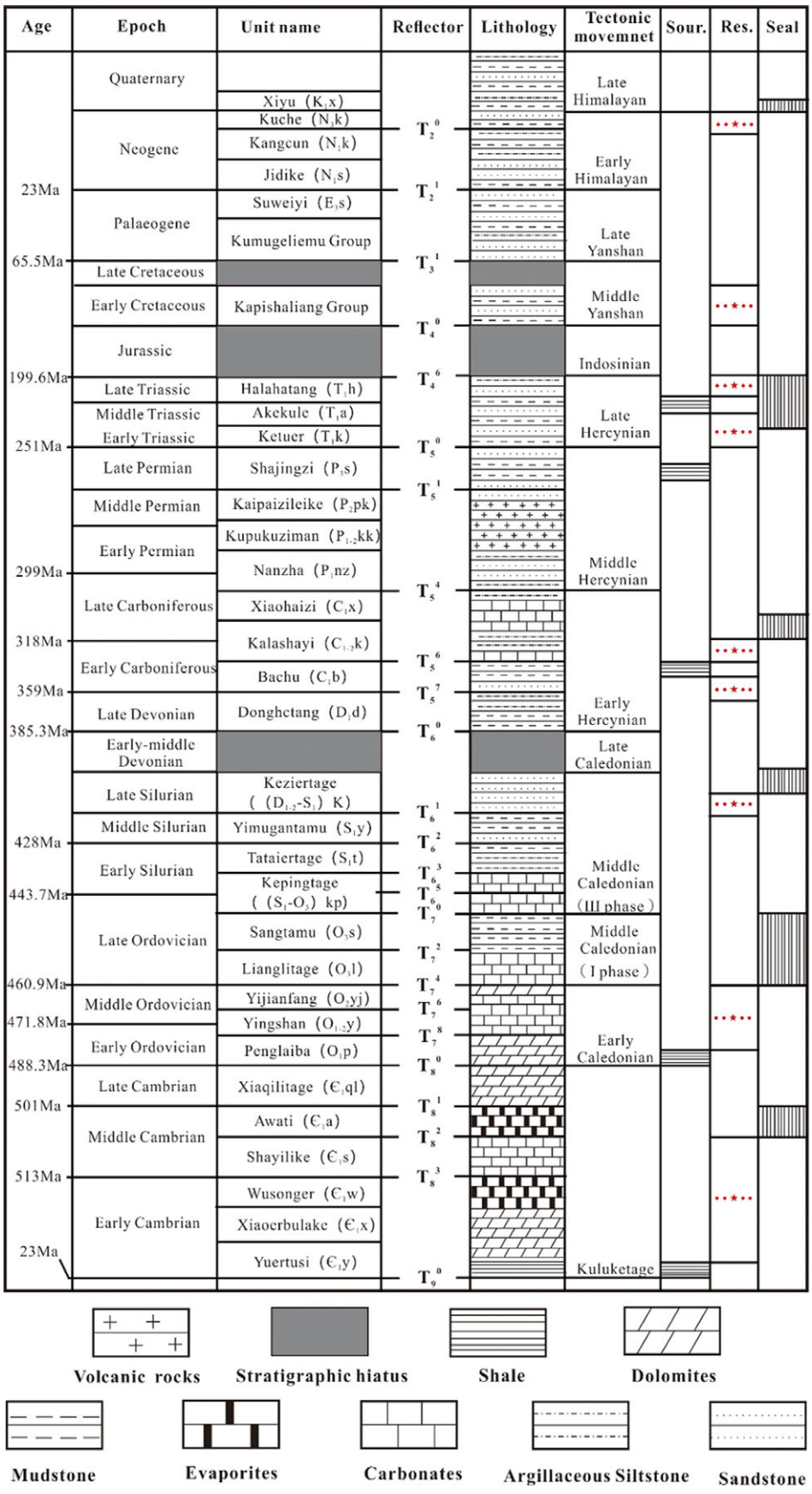

Fig. 2. Stratigraphy of the central Tarim Basin correlated with the seismic reflecting interface (horizons), the timing of regional tectonic movements and petroleum system elements (sources, reservoirs, seals) (modified from Tang *et al.* 2012).

https://doi.org/10.1017/S0016756822000942 Published online by Cambridge University Press

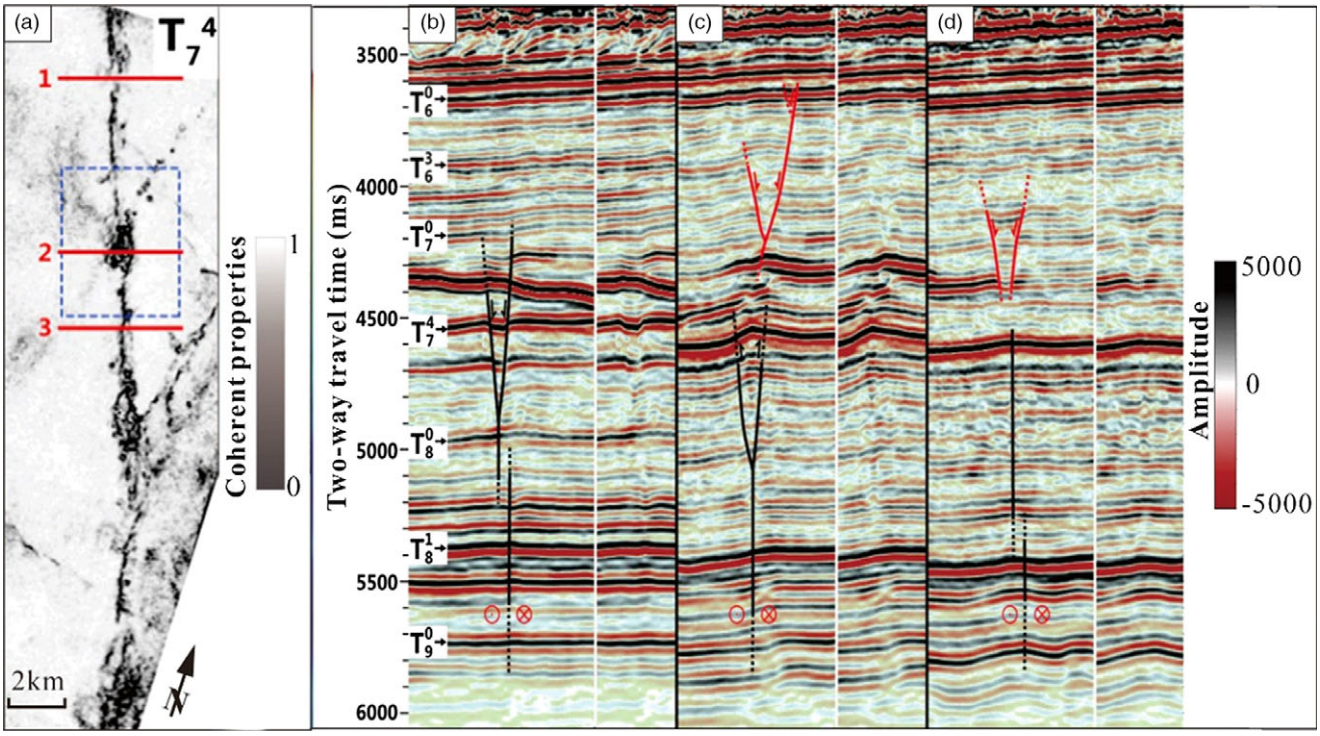

Fig. 3. (a) Plane coherence properties of north section of SB5 fault. (b) Pull-apart segment seismic profile. (c) Uplift segment seismic profile. (d) Translation segment seismic profile.

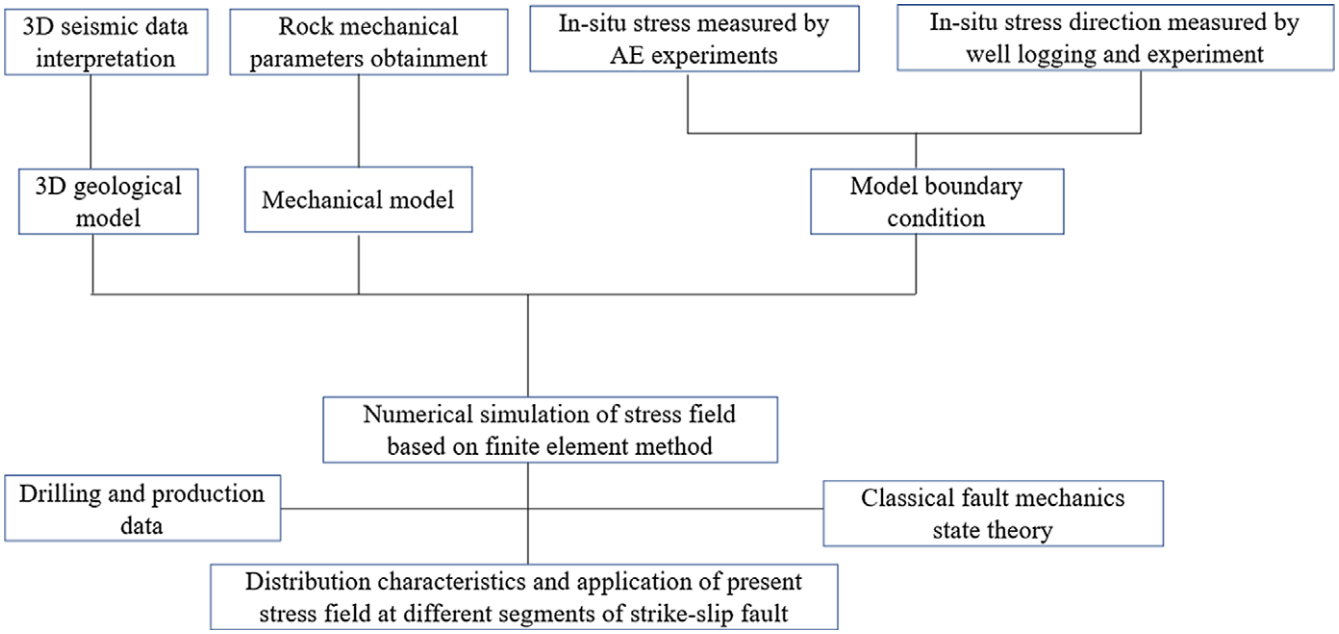

Fig. 4. Adopted workflow to derive the distribution characteristics and application of present *in situ* stress.

$$\sigma_V = \int_0^H \rho(z)g \tag{2}$$

where σ_V (MPa) is vertical stress, H (m) is burial depth and $\rho(z)$ is rock density at burial depth z, which can be acquired from density logging data.

The horizontal principal stress is evaluated by Huang's model, and the evaluation formula is as follows (Yin *et al.* 2017):

$$\sigma_H = \left(\frac{\mu}{1-\mu} + \omega_1\right)(\sigma_V - \alpha P_p) + \alpha P_p \tag{3}$$

$$\sigma_h = \left(\frac{\mu}{1-\mu} + \omega_2\right)(\sigma_V - \alpha P_p) + \alpha P_p \tag{4}$$

where σ_H (MPa) is the maximum horizontal principal stress, σ_h (MPa) is the minimum horizontal principal stress, σ_V (MPa) is

https://doi.org/10.1017/S0016756822000942 Published online by Cambridge University Press

Table 1. Assignment scheme of the rock mechanics parameters in the *in situ* stress simulation

Element type	Density (g cm^{-3})	Young's modulus (GPa)	Poisson's ratio
Fault	2.78	10	0.35
Target layer	2.60	58	0.287
Overburden	5.65	41	0.295

the vertical principal stress, ω_1 and ω_2 are the horizontal *in situ* stress coefficients (the coefficient is obtained by fitting the sample stress obtained by the experiment with the logging curve at the same depth), α is the Biot coefficient, μ is the static Poisson's ratio and P_P (MPa) is the pore pressure.

Present *in situ* stress direction

The present *in situ* stress direction in the T-SH area was based on the present regional *in situ* stress field direction diagram, combined with the borehole breakout method and drilling-induced fracture analysis method (Nelson *et al.* 2005). Analyses of borehole breakout and drilling-induced fractures allow us to infer σ_h and σ_H directions (Zoback *et al.* 2003).

Borehole breakout method

The principle of the borehole breakout method is that the rock around the borehole is affected by the horizontal differential stress to form a breakout phenomenon. The σ_h direction is parallel to the major axis of the ellipse, while the σ_H direction is parallel to the minor axis (Nelson *et al.* 2005)

Drilling-induced fracture analysis method

The principle of the drilling-induced fracture analysis method is that the rock will produce induced fracture under the influence of stress. The drilling-induced fracture strike is consistent with the σ_H direction (Zoback *et al.* 2003).

Results

Present in situ *stress measurement*

Present *in situ* stress direction

The *in situ* stress direction in the T-SH area is roughly NE–SW-trending (Heidbach *et al.* 2016). Due to the influence of fault, different lithology and structure, the *in situ* stress direction varies significantly. In order to accurately determine the present *in situ* stress direction in the T-SH area, the *in situ* stress direction of a single well in the study area was statistically analysed. Through various methods (borehole breakout method, drilling-induced fracture method, wave velocity anisotropy experiment, palaeomagnetic method and dipole acoustic logging data), the *in situ* stress direction of six wells (S1–S6) in the T-SH area was analysed.

Borehole breakout in well S1 (7774.8–7776.0 m, MD) indicated that the σ_H direction is NE25° (Fig. 5a). Borehole breakout in well S2 (7462.3–7464.3 m, MD) indicated that the σ_H direction is NE20° (Fig. 5b). According to the borehole breakout method, the σ_H direction of well S3 (7550.4–7552.4 m, MD) is NE30° (Fig. 5c). The σ_H direction of well S5 (7709.6–7713.2 m, MD) obtained by the borehole breakout method is NE50° (Fig. 5d). In the 7604.4–7606.3 m, MD section of well S1, the drilling-induced fracture rose diagram shows that the strike is NE30°, indicating that the σ_H direction is NE30° (Fig. 5e). The σ_H direction of well S1 obtained by the borehole breakout method and the elliptical borehole method is basically the same. The main strike of the drilling-induced fracture of well S4 is NE60° (Fig. 5f), indicating that the σ_H direction is NE60°.

The palaeomagnetic method and the wave velocity anisotropy method were applied to 11 core samples from well S3. The core samples were taken from the Yijianfang Formation. According to statistics, the σ_H direction is NE74°. According to the anisotropy of wave velocity, the σ_H direction measured in well S6 is NE24.2°. The logging data collected show that the σ_H direction measured by the fast shear wave method in well S4 is NE43.3°.

Due to the influence of fault, lithology and structural characteristics, the σ_H direction measured in each single well changes greatly (Table 2). The direction of *in situ* stress obtained by a single well is consistent with the direction of regional *in situ* stress (NE-trending). Considering that the change of *in situ* stress direction in the study area and the data of σ_H obtained by each single well is small (except for well S3), the average value of these data is taken as the boundary condition of the present *in situ* stress direction (Table 2). Based on these methods, the present maximum horizontal principal stress direction in the T-SH area is NE41.4°, which is consistent with the present maximum horizontal stress direction NE–SW in the T-SH area.

Present *in situ* stress magnitude

In this study, the rock acoustic emission test results of wells S3 and S5 and the logging data calculation results of well S7 are used as reference data to determine the present *in situ* stress magnitude in the T-SH area.

Well S5 is located near the SB5 fault. The experimental samples are cores with well depths of 7656.38–7656.46 m (MD) and 7656.46–7656.57 m (MD), which are within the target layer. The measured σ_V is 189.1 MPa, the σ_H is 191.52 MPa and the σ_h is 141.25 MPa (Table 3). The measured data of well S3 are from the acoustic emission test results of 12 core samples. The test shows that the average σ_V is 182.39 MPa, the average σ_H is 174.73 MPa and the σ_h is 133.27 MPa (Table 3). For the 7650–7690 m (MD) section of well S7, the present *in situ* stress is calculated using poro-elastic formation, and calibrated against the measured point. The present *in situ* stress is composed of rock mass self-weight stress, tectonic movement stress, fluid seepage stress and other stresses (geothermal, geochemical, etc.). The calculated average σ_V is 181.4 MPa, the average σ_H is 167.1 MPa and the σ_h is 136.5 MPa (Fig. 6). Based on these analysis and test results, the average σ_V is 184.57 MPa, the average σ_H is 177.78 MPa and the σ_h is 137.01 MPa (Table 3). The present *in situ* stress in the T-SH area is defined as the loading boundary condition.

Present *in situ* stress field simulation

The primary steps of the 3D FEM include model-building, rock mechanical parameter assignment, meshing, stress loading, calculation and result analysis.

Model-building

The geological model takes the T_7^4 interface (the top of the Ordovician Yijianfang Formation) as the top surface, and the layer depth is 1000 m. The depth of the T_7^4 interface is determined according to the contour map of the northern section of the SB5 fault (Fig. 7). The model considers the attitude and style of the northern section of the SB5 fault (Fig. 8a, b). In order to consider the stress effect of the overlying formation on the target layer, an

https://doi.org/10.1017/S0016756822000942 Published online by Cambridge University Press

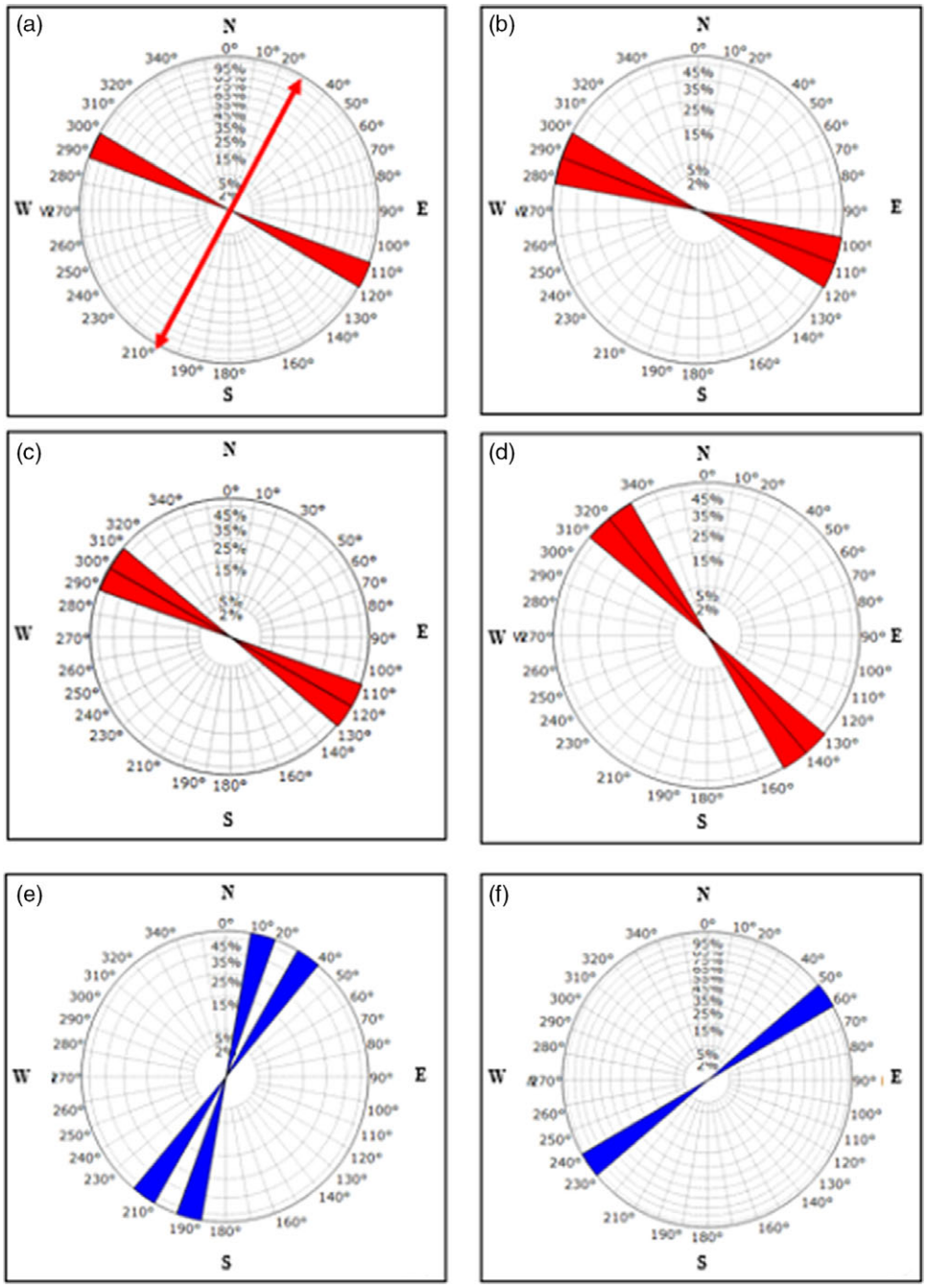

Fig. 5. Analysis of present *in situ* stress direction. (a) Borehole breakout direction of well S1 (7774.8–7776.0 m); (b) borehole breakout direction of well S2 (7462.3–7464.3 m); (c) borehole breakout direction of well S3 (7550.4–7552.4 m); (d) borehole breakout direction of well S5 (7709.6–7713.2 m); (e) strike of drilling-induced fracture in well S1 (7604.4–7606.3 m); (f) strike of drilling-induced fracture in well S4 (7710.7–7712.9 m).

overburden from the surface to the buried depth of 9000 m is established. The purpose of the overburden is to realize the loading of vertical stress (gravity).

To establish the geological model of the fault, firstly, according to the plane coherence properties (Fig. 3a), the key breakpoints of the fault were selected on the equidistant survey line. The X, Y and Z coordinates of the breakpoints were determined and imported into software to restore the strike and dip angle of the fault. Secondly, based on the interpretation of the corresponding seismic profile (Fig. 3b–d), we could clearly identify the dip direction. Combined with plane coherence properties and seismic profile, the occurrence of the northern section of the SB5 fault is inputted in software. For the formation near the fault, 50 equidistant data points with three-axis coordinates were derived from the contour map of the T_7^4 interface (Fig. 7) in the X and Y directions. A total of 2500 data points were imported into the software and combined to form a whole, which has the actual buried depth. After these two kinds of geological models were established, the formation and fault were combined by overlap operation in the software (Fig. 8a, b).

Rock mechanics parameter assignments

The geological model of the northern section of the SB5 fault has established three types of units: fault, formation near the fault and overburden.

The fault is composed of fault gouge and broken breccia (Billi *et al.* 2003), and drilling results show that the SB5 fault has this characteristic. It is difficult to obtain samples inside the fault to carry out mechanical parameter experiments. Because the rock

https://doi.org/10.1017/S0016756822000942 Published online by Cambridge University Press

Table 2. Statistics of the maximum horizontal stress direction for wells S1–S6 in the T-SH area

Well	Method	σ_H direction
S1	Drilling-induced fracture; borehole breakout	NE30°
S2	Borehole breakout	NE20°
S3	Borehole breakout	NE30°
S4	Drilling-induced fracture; borehole breakout	NE60°
S5	Borehole breakout	NE50°
S6	Palaeomagnetic	NE74°
S4	Wave velocity anisotropy	NE43.3°
S3	Palaeomagnetic, wave velocity anisotropy	NE24.2°
Average value		NE41.4°

Table 3. Present *in situ* stress test and calculation results for wells S3, S5 and S7

Well	Method	σ_V (MPa)	σ_H (MPa)	σ_h (MPa)
S3	AE	182.39	174.73	133.27
S5	AE	189.91	191.52	141.25
S7	Logging calculation	181.4	167.1	136.5
Average value		184.57	177.78	137.01

strength inside the fault is low, this simulation refers to the rock mechanics parameters of mudstone. The Young's modulus and Poisson's ratio of the fault are 10 GPa and 0.35 respectively.

The target formation is an ultra-deep formation (>6000 m) with high temperature and pressure. In order to achieve the real geological conditions, the samples used were those with confining pressure of 60 MPa and temperature of 140 °C in well S3 (Table 4). According to the selected sample data, the average value was taken as the rock mechanics parameters of the formation near the fault. The Young's modulus is 58 GPa and the Poisson's ratio is 0.287.

The overburden can be regarded as a geological body from the surface to 9000 m underground, and the overall temperature and pressure conditions are lower than those of ultra-deep formation. Therefore, the samples with confining pressure of 15 MPa and temperature of 30 °C in well S5 were selected as rock mechanics parameters (Table 5). The Young's modulus and Poisson's ratio of the overburden are 41 GPa and 0.295 respectively. The fault and target formation are embedded into this overburden.

Meshing

A key parameter of FEM is mesh generation. After determining the rock mechanics parameters and establishing the geomechanical model, according to the strain characteristics of different rocks different types of grid elements are selected for the division of geomechanical models to obtain the finite-element model. For the T-SH area, the Solid95 element is selected to grid the geological model. The Solid95 element constructs a 3D finite-element model through 20 nodes, each node having three degrees of freedom in the X, Y and Z directions, and the element has the capabilities of plasticity, creep, expansion, stress strengthening, large deformation and large strain, which is closest to the actual geological body (Sun *et al.* 2019). In the process of meshing, different models should be given different grid lengths. In order to more finely reflect the stress distribution of the strike-slip fault, the grid length of the strike-slip fault is smaller than that of the formation. The geological model (fault and formation) of the north section of the SB5 fault constitutes 94 444 elements and 142 218 nodes.

Based on the establishment of the geological model and determination of various rock mechanics parameters, the model can be loaded and solved according to the present *in situ* stress direction. The vertical direction of the model is Z-axis upward. The X-axis trends E–W, and the Y-axis N–S.

Distribution of the present in situ stress

Based on the requirements of FEM computation (the model has no overall translation and rotation, and can calculate and obtain the convergence solution), the loading conditions are imposed on the model (Fig. 8c). The loading method is to constrain the bottom surface of the footwall of the model and fix its displacement in the Z direction, which can reduce the deformation of the footwall base rock. The applied boundary forces include horizontal tectonic force and gravity. The σ_h and σ_H direction for loading at overburden are SE131.4°–NW311.4° and NE41.4°–SW221.4°, and the σ_h and σ_H magnitudes for loading at overburden are 137.01 MPa and 177.78 MPa. In the vertical direction, the loading stress is gravity, and the loading method is to apply the gravity acceleration of 9.8 N kg^{-1} on the overburden.

The distributions of the present *in situ* stress of the target formation are shown in Figure 9. The range of σ_1 in the formation around the strike-slip fault is 185 –195 MPa, the range of σ_3 in the uplift segment is 180 –190 MPa and the value of σ_1 near the strike-slip fault is larger than 200 MPa. The range of σ_2 in the formation around the strike-slip fault is 163–177 MPa, and the range of σ_1 in the uplift segment is 150 –165 MPa. The range of σ_3 in the formation around the strike-slip fault is 130 –145 MPa, the range of σ_3 in the uplift segment is 130 –135 MPa and the value of σ_1 near the strike-slip fault is larger than 150 MPa.

Discussion

Distribution of present in situ stress

The σ_1 direction near the strike-slip fault is vertical. However, the σ_1 direction in the uplift segment is horizontal. In seismic section, compared with the surrounding formation, the uplift amplitude of the uplift segment is larger than 20 ms, and the maximum value can exceed 60 ms. The reason for the change of stress direction is that the buried depth of the uplift segment in the strike-slip fault is shallower than that of the nearby formation. The horizontal stress is larger than the vertical stress in shallow formation. Brown & Hoek (1978) provided statistics on the distribution law of the ratio of the global measured horizontal average principal stress to the vertical stress with the buried depth, as shown in the formula

$$\frac{100}{H} + 0.3 \leq \frac{\sigma_H + \sigma_h}{2\sigma_V} \leq \frac{1500}{H} + 0.5 \quad (5)$$

where σ_H (MPa) is the maximum horizontal principal stress, σ_h (MPa) is the minimum horizontal principal stress (MPa), σ_V (MPa) is the vertical principal stress and H (m) is buried depth.

https://doi.org/10.1017/S0016756822000942 Published online by Cambridge University Press

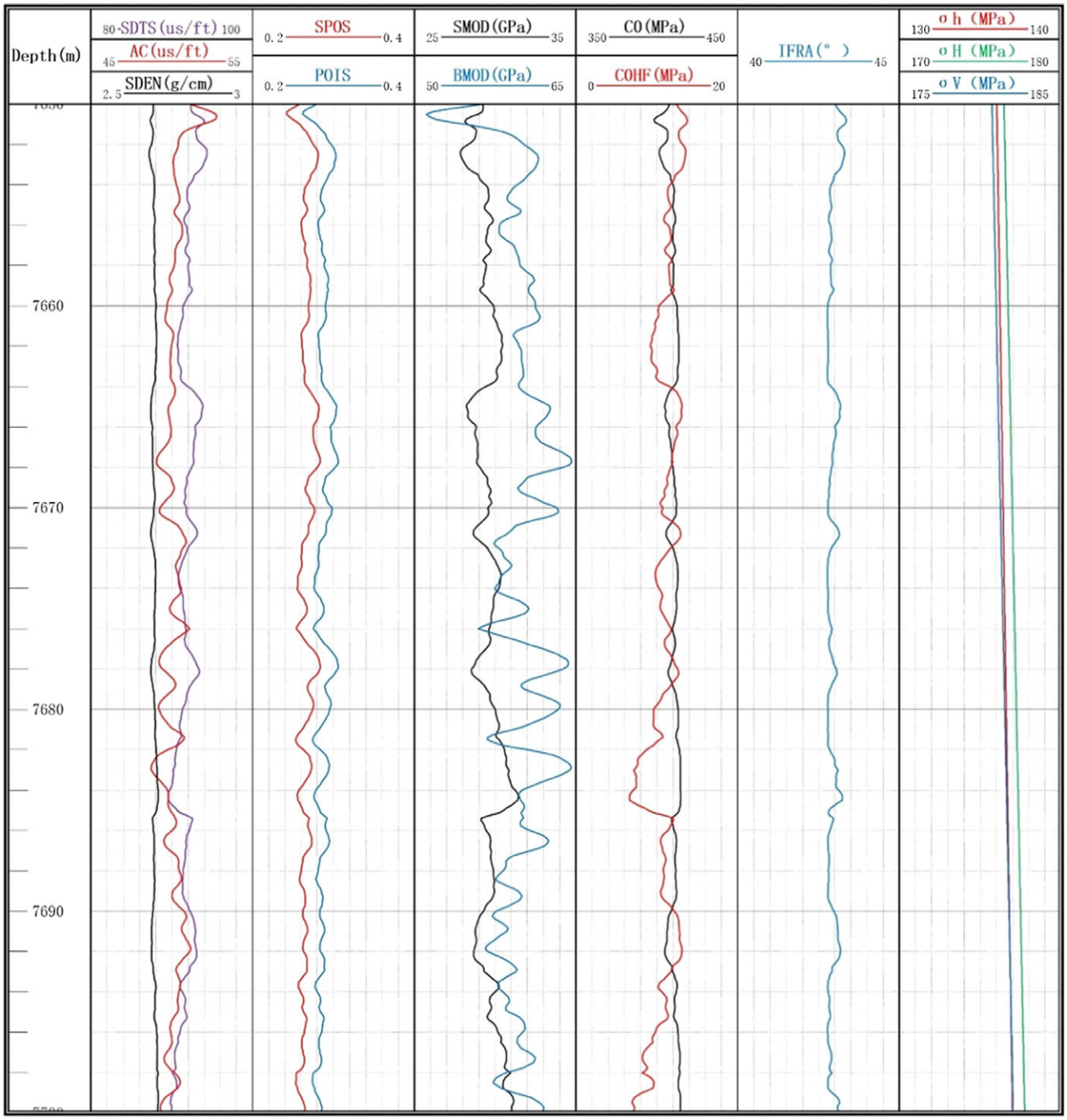

Fig. 6. Calculation of present *in situ* stress using conventional logging (acoustic logging, density logging) of well S7 (7650–7690 m). Column 1: shear sonic, acoustic and density logs; column 2: static Poisson's ratio and Poisson's ratio; column 3: shear modulus and bulk modulus; column 4: compressive strength and cohesive force; column 5: internal friction angle; column 6: minimum horizontal principal stress, maximum horizontal principal stress and vertical principal stress.

The Anderson fault formation mechanism describes the mechanical state of different faults (Anderson, 1951). The fault primarily formed under a strike-stress regime, forming the strike-slip fault system. A change of stress state occurred in time, resulting in reactivating the system under a normal stress regime. According to the Anderson model, it is found that the strike-slip fault of the target layer in the T-SH area is now in the normal fault stress state, and the horizontal compression is significant. For the uplift segment, it is in a state of strike-slip stress, and the horizontal compression is more significant.

It is well established that fault perturbations will tend to deflect the stress in a certain trend (Husodon & Cooling, 1988). Numerical analysis methods such as finite element (Matsukik *et al.* 2009; Bouatia *et al.* 2020), discrete element (Stephansson & Zang, 2012) and boundary element (Zhong *et al.* 2010) were also used to study the disturbance law of fault to local stress field.

Based on the borehole breakout method, the drilling-induced fracture method, palaeomagnetic experiment and wave velocity anisotropy analysis, it is determined that the average σ_H direction in the T-SH area is NE41.1° (Table 3). The finite-element numeri-

https://doi.org/10.1017/S0016756822000942 Published online by Cambridge University Press

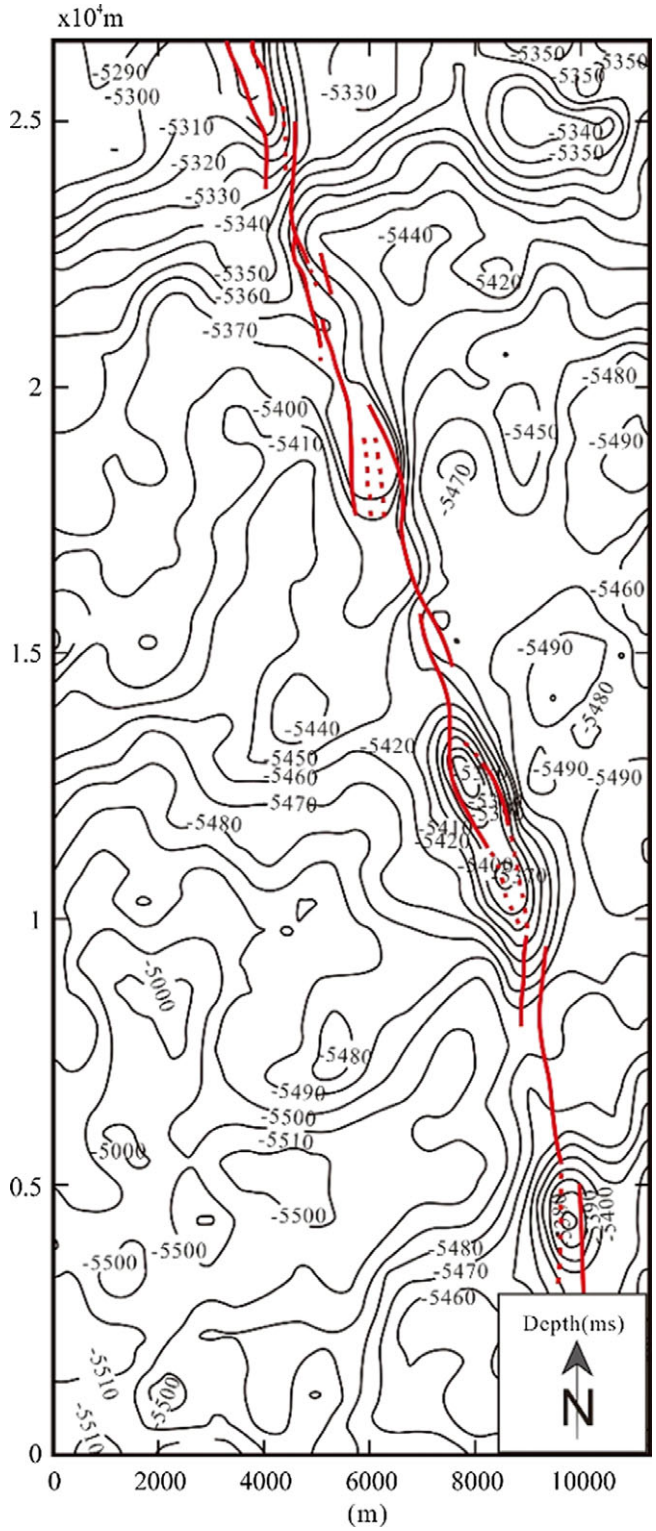

Fig. 7. Present buried depth map of T_7^4 interface in the northern section of the SB5 fault.

cal simulation of the maximum horizontal principal stress direction in the northern section of the SB5 fault is carried out using ANSYS software to study whether the fault interactions will perturb the stress orientation. The simulation results show that the σ_2 direction near the strike-slip fault is horizontal and the overall direction is NE–SW-trending. In the formation near the strike-slip fault, there is no obvious change in the σ_2 direction, which is consistent with the measured data. Near the strike-slip fault, the σ_2 direction deflects, and the closer it is to the fault, the greater the angular deflection. The deflection of the σ_2 direction has a trend parallel to the strike of the fault (Fig. 10a). For the uplift segment, in the nearby formation, the σ_2 direction is horizontal, which is consistent with the regional stress field direction. Near the fault, the σ_2 direction deflects anticlockwise, which is parallel to the strike of the fault. In the uplift segment, the σ_2 direction is vertical and the σ_3 direction is horizontal (Fig. 10b). The uplift segment is a structural high part formed under the combined action of shear stress along the fault strike direction and compressive stress. The buried depth is relatively shallow with the surrounding formation. The horizontal principal stress of the shallow buried formation is generally higher than the vertical principal stress (Brown & Hoek, 1978).

In situ stress partitioning into several segments

Using the numerical simulation results for the northern section of the SB5 fault, the triaxial principal stress and stress anomaly range of the uplift segment, pull-apart segment and translation segment are compared (Fig. 11; Table 6). In each segment, the stress can be divided into three parts: inside the fault, inside the segment and near the fault. The stress differences for each of these three parts are compared. Inside the fault, the *in situ* stress magnitude of the three segments is smaller than that in the surrounding formation. The smaller value is similar in the three segments. Inside the segment, the *in situ* stress in the uplift segment and pull-apart segment is smaller than that in the surrounding formation. This is related to the fault activity and the mechanical property changes between the three deformation types and the surrounding formation. Near the fault, the σ_1 and σ_3 magnitude in the three segments is larger than that in the surrounding formation, the σ_2 magnitude in the three segments is smaller than that in the surrounding formation. Although the abnormal values near different segmented faults are slightly different, the variation is the same. For the range of abnormal stress, the uplift segment is 250–300 m, the pull-apart segment is 150–300 m and the translation segment is 100–250 m. The overall anomaly range is largest in the uplift segment, next largest in the pull-apart segment and smallest in the translation segment.

Present *in situ* stress application

Hydraulic fracturing

Rock is in a complex stress state composed of overlying formation pressure, tectonic stress, wall rock pressure and pore fluid pressure (Aadnoy, 1989; Marques *et al.* 2018). Due to the difference of *in situ* stress state, the rock has different fracture propagation patterns, resulting in the formation of a variety of fractures with different properties and occurrence (Schultz, 2000; Griffith *et al.* 2014; Lee *et al.* 2018). The present *in situ* stress state directly controls the occurrence and propagation trending of fractures produced by acid fracturing (K Zhao *et al.* 2021).

According to the formation conditions, fractures can be divided into three types: shear fractures, tension fractures and mixed modes (Zhu & Song, 1990; Zeng *et al.* 2007). The *in situ* stress controlling the formation of shear fractures is compressive stress, generally as a conjugate set of two fractures. The tensile fracture also has the characteristics of displacement direction perpendicular to and away from the fracture surface, and the minimum principal stress direction is perpendicular to the fracture surface, but the

https://doi.org/10.1017/S0016756822000942 Published online by Cambridge University Press

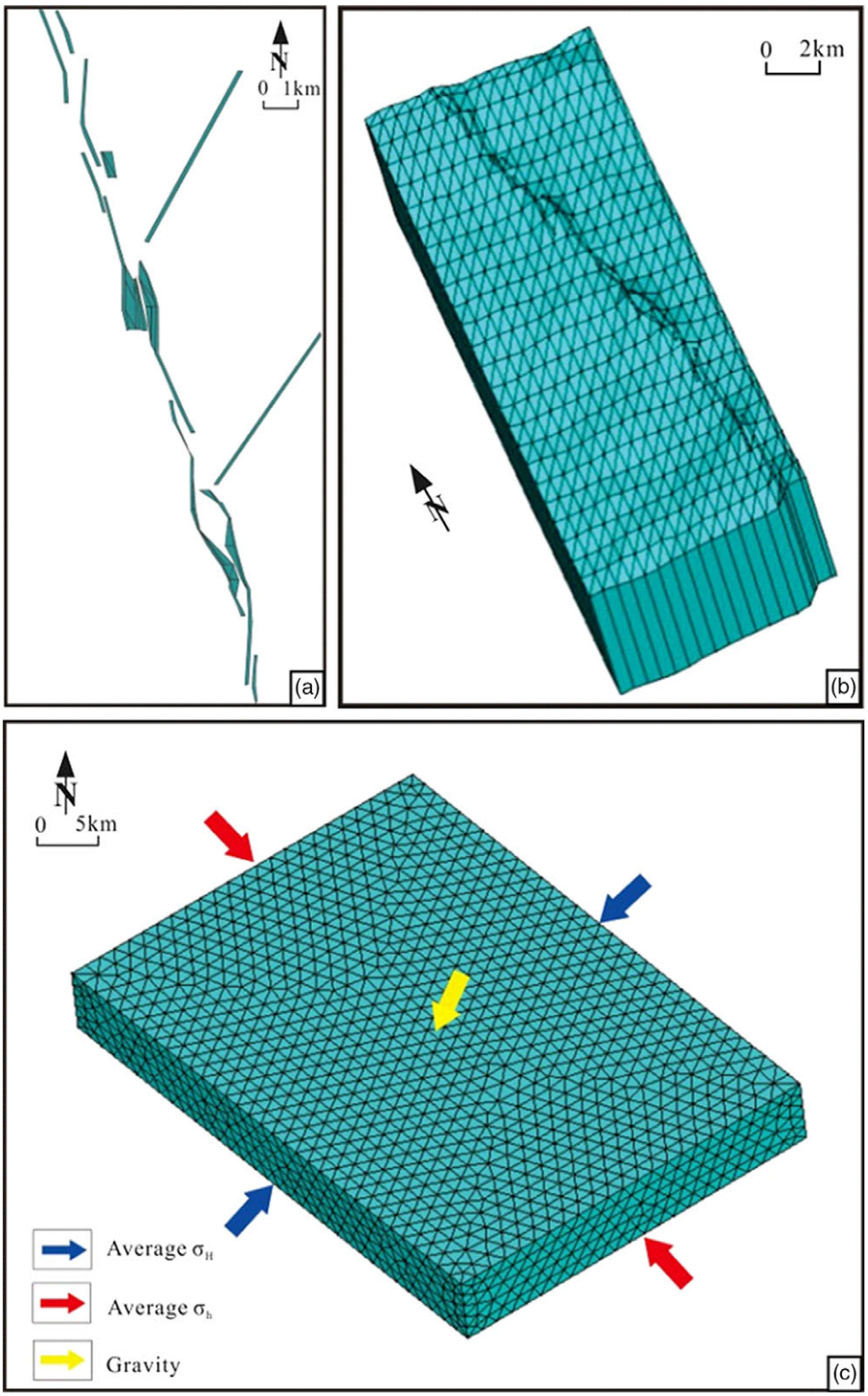

Fig. 8. (a) 3D strike-slip fault model. (b) 3D strike-slip fault and target layer model. (c) Boundary conditions of stress simulation of the northern section of the SB5 fault.

basic condition for forming the tensile crack is that at least one principal stress is the tensile stress.

The numerical simulation results show that the present *in situ* stress along the target formation of the SB5 fault is compressive stress. Therefore, the fractures produced by acid fracturing are mainly shear fractures, tensile fractures cannot be produced and the fracture surface is perpendicular or approximately perpendicular to the σ_3 direction. The σ_3 direction in the T-SH area is NW–SE-trending, resulting in high-angle fractures from acid fracturing. The propagation direction of hydraulic fractures is consistent with the σ_2 direction. Along the SB5 fault, except for the uplift segment, the present *in situ* stress state is: vertical σ_1, NE–SW-trending σ_2 and NW–SE-trending σ_3 (Figs 12d, 11e–i). Therefore, the fractures due to acid fracturing are mainly high-angle fractures, and

https://doi.org/10.1017/S0016756822000942 Published online by Cambridge University Press

Table 4. Evaluation of the experimental results of rock mechanics in well S3

Sample number	Depth (m)	Confining pressure (MPa)	Temperature (°)	Young's modulus (GPa)	Poisson's ratio
1	7516.05–7516.19	60	140	53	0.243
2	7522.56–7522.73	60	140	68	0.329
3	7528.99–7529.14	60	140	54	0.289
Average value				58	0.287

Table 5. Evaluation of the experimental results of rock mechanics in well S5

Sample number	Depth (m)	Confining pressure (MPa)	Temperature (°)	Young's modulus (GPa)	Poisson's ratio
1	7653.73–7653.81	15	30	41	0.276
2	7653.41–7653.55	15	30	40	0.347
3	7652.00–7652.14	15	30	42	0.262
Average value				41	0.295

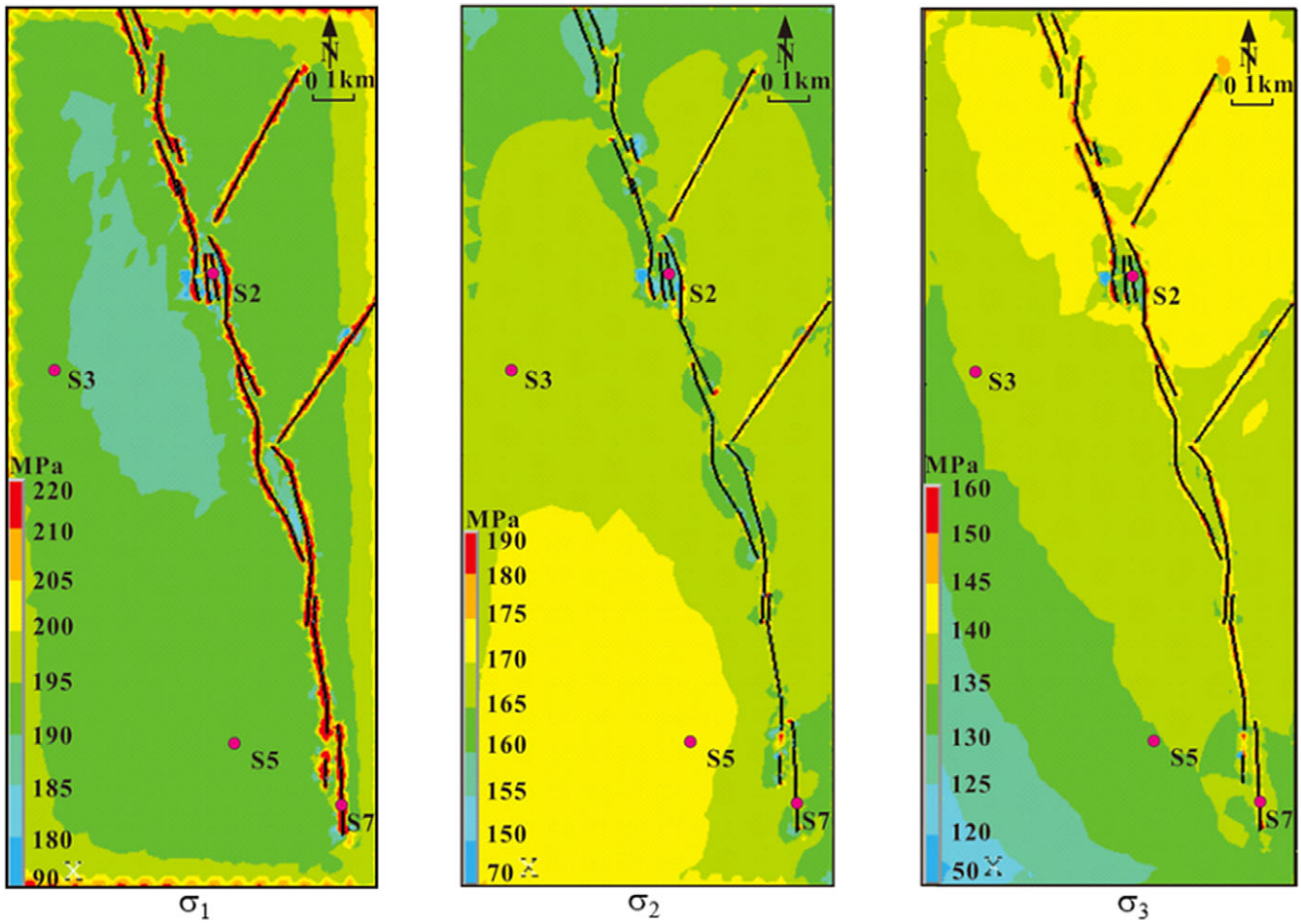

Fig. 9. Present triaxial stress magnitude in the northern section of the SB5 fault.

the main propagation direction is NE–SW-trending (Fig. 13a). This kind of fracture has stronger horizontal communication ability and communicates more easily with multiple sets of fault–fracture reservoirs. The present *in situ* stress state in the uplift segment is: NE–SW-trending σ_1, vertical σ_2 and NW–SE-trending σ_3 (Fig. 12a–c). Under the control of such a stress state, although the fractures produced by acid fracturing are mainly high-angle fractures, their propagation direction is mainly longitudinal (vertical) (Fig. 13b). This type of fracture communicates more easily with deep reservoirs.

https://doi.org/10.1017/S0016756822000942 Published online by Cambridge University Press

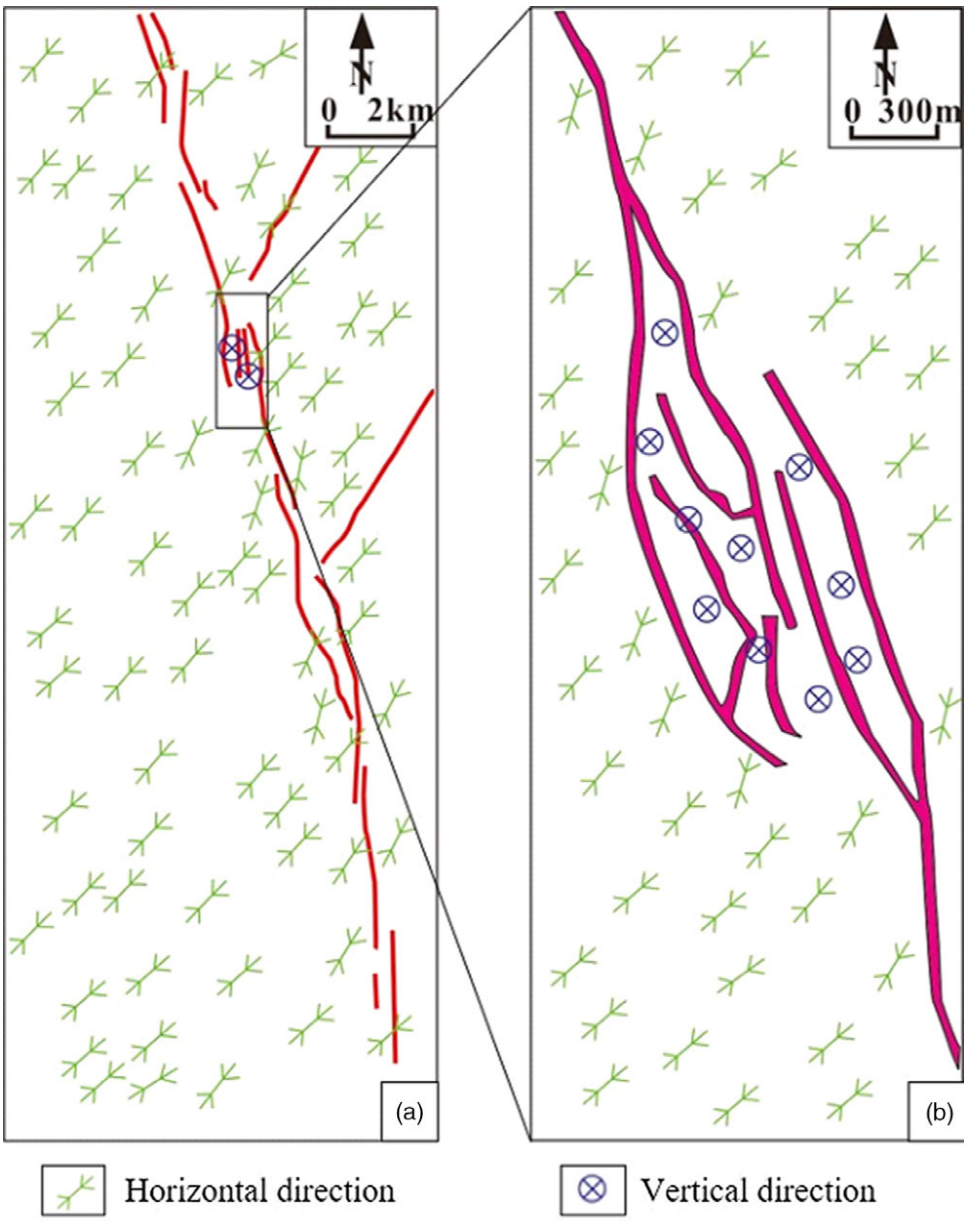

Fig. 10. Characterization of σ_2 in (a) the northern section of the SB5 fault and (b) the uplift segment. As shown, σ_2 starts deflecting from NE–SW-trending when approaching the strike-slip fault, until it switches from the horizontal to the vertical within the uplift segment.

Effectiveness evaluation of natural fractures

Present *in situ* stress not only controls the propagation trend of fractures from acid fracturing, but also controls the opening trend of pre-existing natural faults and fractures. The smaller the angle between the natural fracture strike and the σ_H direction, the easier it is to open (Angelier *et al.* 2004; Zoback, 2007; Angelier & Baruah, 2009; Zhao *et al.* 2020). Based on the numerical simulation of the present *in situ* stress field in the SB5 fault, the opening trend of the fault and fracture can be qualitatively evaluated. In this study, the natural fault–fracture opening trend of well S2 is qualitatively evaluated.

Well S2 has conducted four sidetracks: three of these are NE-trending, and mainly intersected NW–SE-trending faults and fractures, whilst the fourth sidetrack is NE-trending and mainly intersected NE–SW-trending faults and fractures.

A total of 21 fractures were identified by image logging; their strikes were both NE–SW-trending and NW–SE-trending, with the two sets showing both low and high dip angles (Fig. 14). The three sidetracks mainly encountered NW–SE-trending faults and fractures, with only a small total hydrocarbon display. The fourth sidetrack intersected mostly low-angle NE–SW-trending fractures, with larger total hydrocarbon display (Fig. 15). This is consistent with the medium–high permeability values (up to 162 md) of the formation. The σ_H direction is NE–SW-trending. Under this condition, NW–SE-trending fractures do not open, but NE–SW-trending fractures open, resulting in a larger display of total hydrocarbons. Therefore, present *in situ* stress direction can be used to evaluate the effectiveness of natural faults and fractures, and then provide a basis for drilling trajectory optimization and reservoir reconstruction measures.

Conclusion

In the T-SH area, the σ_1 magnitude is 185 –195 MPa, the σ_2 magnitude is 163 –177 MPa and the σ_3 magnitude is 130–145 MPa. For strike-slip fault and surrounding formation, the σ_1 direction is vertical, and the σ_2 and σ_3 directions are horizontal, belonging to a normal fault stress

https://doi.org/10.1017/S0016756822000942 Published online by Cambridge University Press

Table 6. Statistics of triaxial principal stress anomalies along different strain segments of the SB5 fault

Segment type	Uplift segment			Pull-apart segment			Translation segment		
Triaxial stress	σ_1	σ_2	σ_3	σ_1	σ_2	σ_3	σ_1	σ_2	σ_3
Inside fault	12 MPa↓	8 MPa↓	12 MPa↓	4 MPa↓	8 MPa↓	12 MPa↓	16 MPa↓	8 MPa↓	8 MPa↓
Inside segment	12 MPa↓	4 MPa↓	8 MPa↓	4 MPa↓	4 MPa↓				
Near fault	16 MPa↑	20 MPa↓	12 MPa↑	20 MPa↑	16 MPa↓	12 MPa↑	8 MPa↑	15 MPa↓	16 MPa↑
Influence range	300 m	250 m	280 m	220 m	150 m	300 m	150 m	100 m	250 m

Notes: ↑ indicates that the stress is more than the principal stress of the surrounding formation; ↓ indicates that it is less than the stress of the surrounding formation.

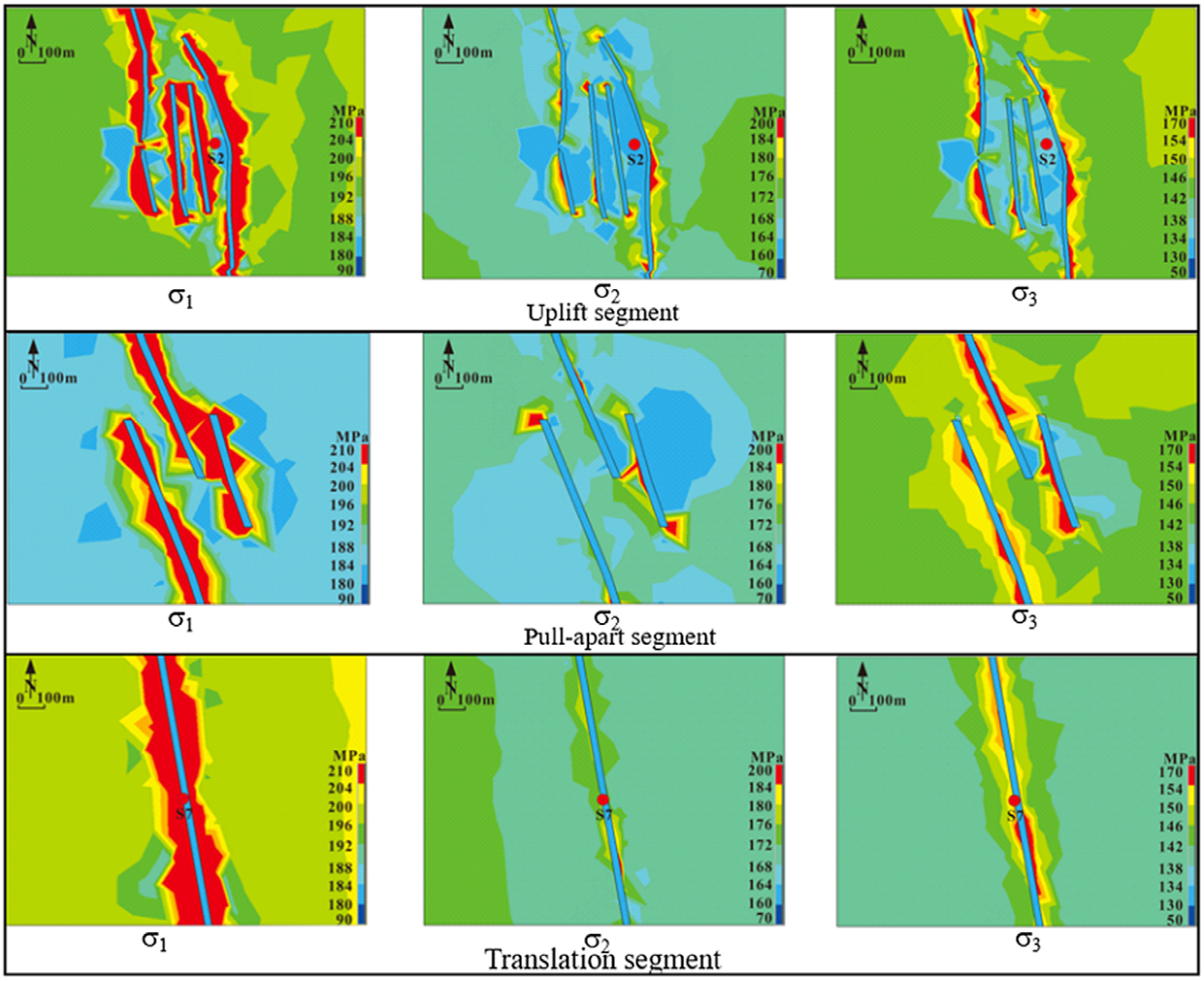

Fig. 11. Triaxial principal stress distribution of different strain segments along the SB5 fault.

state. For the uplift segment, due to the relatively low buried depth, the σ_2 direction is vertical and the σ_1 and σ_3 directions are horizontal, belonging to a strike-slip fault stress state.

The average σ_H direction in the T-SH area is NE41.1°. With the existence of a strike-slip fault, the σ_H direction will deflect. The σ_H direction near the fault tends to be consistent with the fault strike.

The segmentation of the strike-slip fault has only local influence on the present *in situ* stress. The present stress field is mainly affected by the shape, scale and quantity of pre-existing faults. It is shown that the triaxial principal stress is relatively small as a whole, and the range of stress anomaly is slightly different, being 2–6 times the width of the fault. The abnormal range of the uplift

https://doi.org/10.1017/S0016756822000942 Published online by Cambridge University Press

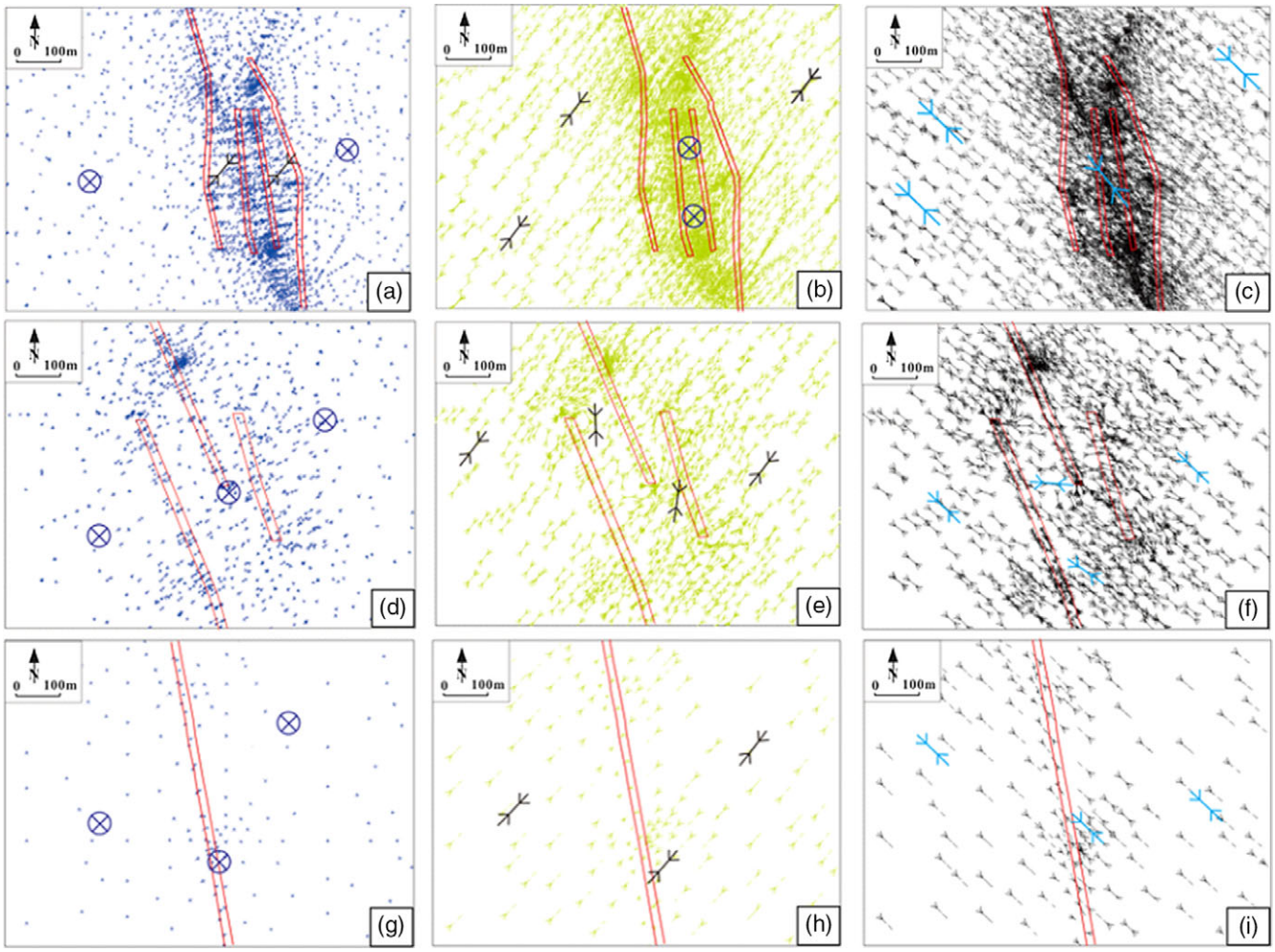

Fig. 12. (a) σ_1 direction in the uplift segment; the exterior is vertical, the interior is NE–SW-trending. (b) σ_2 direction in the uplift segment; the exterior is NE–SW-trending, the interior is vertical. (c) σ_3 direction in the uplift segment; the whole is NW–SE-trending. (d) σ_1 direction in the pull-apart segment; the whole is vertical. (e) σ_2 direction in the pull-apart segment; the whole is NE–SW-trending. (f) σ_3 direction in the pull-apart segment; the whole is NW–SE-trending. (g) σ_1 direction in the translation segment; the whole is vertical. (h) σ_2 direction in the translation segment; the whole is NE–SW-trending. (i) σ_3 direction in the translation segment; the whole is NW–SE-trending.

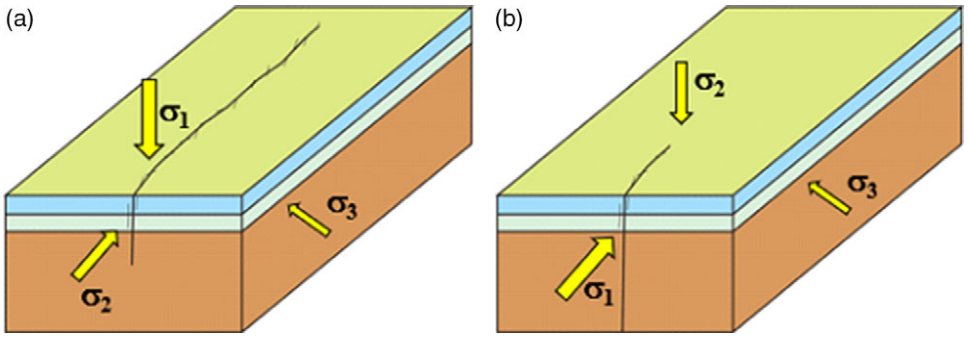

Fig. 13. Propagation mode for fractures from acid fracturing under different stress conditions along the SB5 fault. (a) σ_2 direction is horizontal; high-angle fracture propagates along horizontal direction. (b) σ_2 direction is vertical; high-angle fracture propagates along horizontal direction.

segment is the largest, the pull-apart segment is second largest and the translation segment is smallest.

Controlled by the present *in situ* stress, the propagation trend of fractures is different in different areas. In the uplift segment, the σ_1 direction is horizontal, and the fractures caused by acid fracturing mainly extended vertically. This type of fracture allows easier communication with the deep reservoir. In other areas, the σ_1 direction is vertical and the propagation direction of high-angle fractures caused by acid fracturing is NE–SW-trending. This kind of fracture has strong horizontal communication ability, and is therefore able to improve connectivity amongst fault–fracture reservoirs.

The smaller the angle between the natural fracture strike and the σ_H direction, the easier it is to open. Therefore, present *in situ* stress direction can be used to qualitatively evaluate the effectiveness of natural fractures, so as to provide a basis for drilling-trajectory optimization and reservoir reconstruction measures.

https://doi.org/10.1017/S0016756822000942 Published online by Cambridge University Press

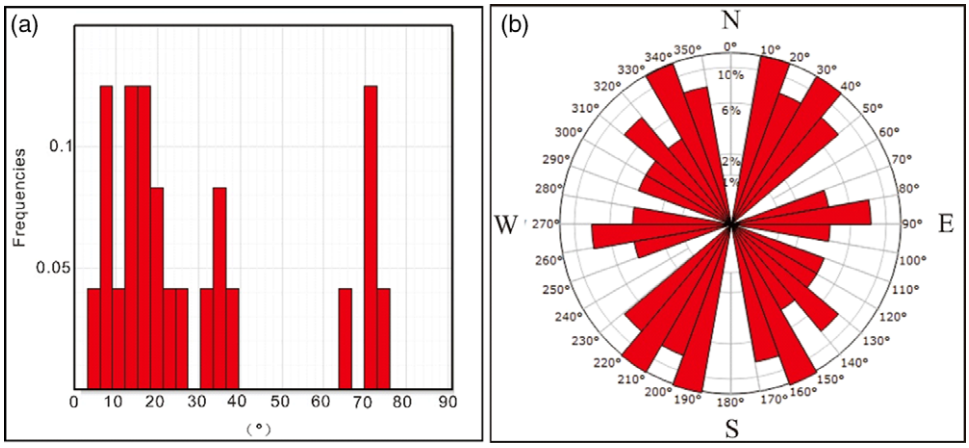

Fig. 14. Dip angles (a) and strikes (b) of fractures encountered by well S2.

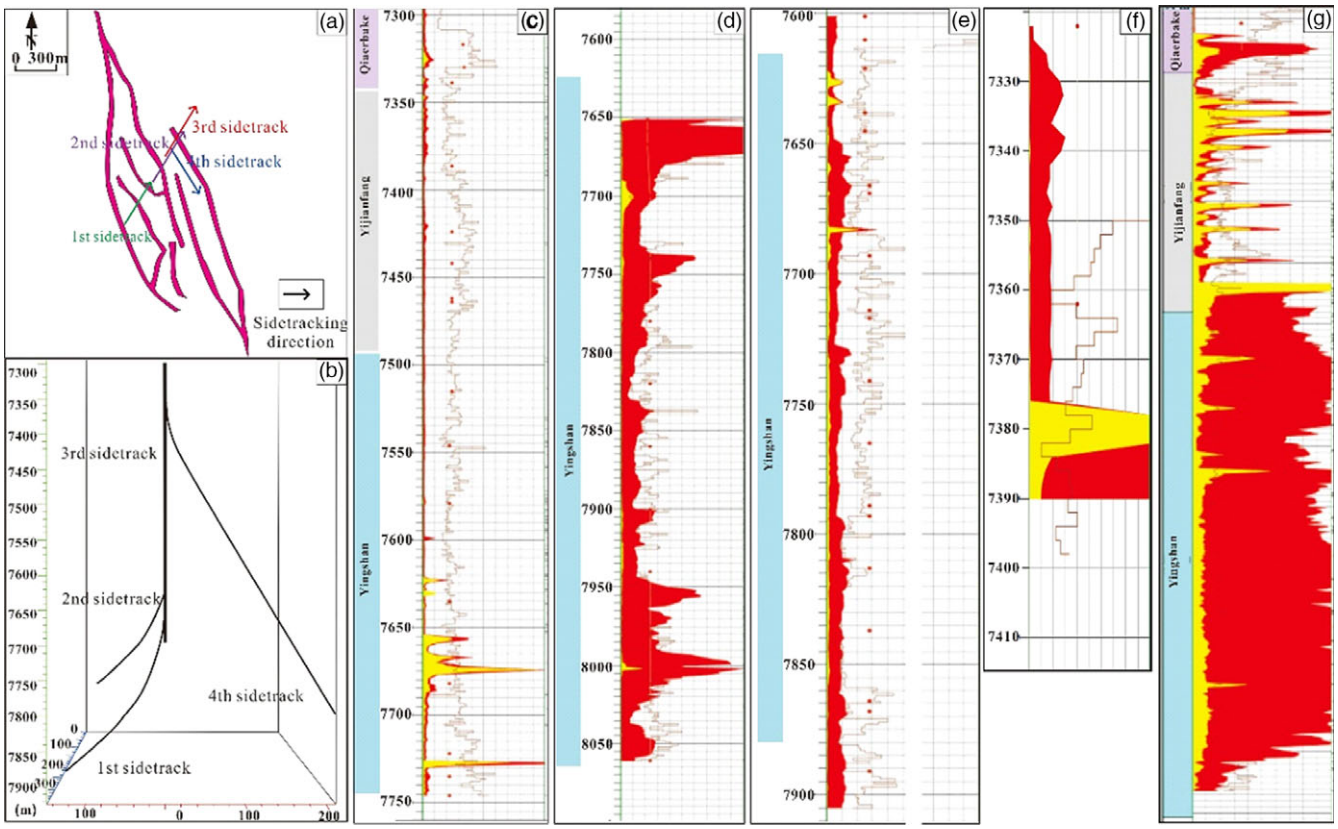

Fig. 15. (a) Sidetrack directions of well S2 in map view. (b) Vertical borehole S2 and the four sidetracks with different directions. (c) Hydrocarbon shows for the vertical well. (d–g) Hydrocarbon displays for the four sidetracks.

Acknowledgements. This work was financially supported by the National Natural Science Foundation of China (NSFC) (Grant No. 42072173) and the Joint fund for enterprise innovation and development of National Natural Science Foundation of China 'Study on enrichment mechanism and key engineering technology of marine deep oil and gas' (U19B6003). Dr Ahmed E Radwan thanks the Priority Research Area Anthropocene under the program 'Excellence Initiative—Research University' at the Jagiellonian University in Kraków.

Conflict of interest. The authors declare that they have no known competing financial interests or personal relationships that could have appeared to influence the work reported in this paper.

References

Aadnoy BS (1989) Stresses around horizontal boreholes drilled in sedimentary rocks. *Journal of Petroleum Science & Engineering* **2**, 349–60. doi: 10.1016/0920-4105(89)90009-0.

Alsop I (2009) Tectonics of strike-slip restraining and releasing bends. *Geological Magazine* **146**, 781–82. doi: 10.1017/S0016756809006025.

Anderson EM (1951) *The Dynamics of Faulting*, 2nd edn. London: Oliver and Boyd, 206 pp. doi: 10.1144/transed.8.3.387.

Angelier J and Baruah S (2009) Seismotectonics in northeast India: a stress analysis of focal mechanism solutions of earthquakes and its kinematic implications. *Geophysical Journal International* **178**, 303–26. doi: 10.1111/j.1365-246X.2009.04107.x.

Angelier J, Slunga R, Bergerat F, Stefansson R and Homberg C (2004) Perturbation of stress and oceanic rift extension across transform faults shown by earthquake focal mechanisms in Iceland. *Earth & Planetary Science Letters* **219**, 271–84. doi: 10.1016/S0012-821X(03)00704-0.

Bahorich M and Farmer S (1995) 3-D seismic discontinuity for faults and stratigraphic features: the coherence cube. *Leading Edge* **14**, 1053–8.

Bertoluzza L and Perotti CR (1997) A finite-element model of the stress field in strike-slip basins: implications for the Permian tectonics of the Southern Alps (Italy). *Tectonophysics* **280**, 185–97. doi: 10.1016/S0040-1951(97)00140-6.

Billi A, Salvini F and Storti F (2003) The damage zone-fault core transition in carbonate rocks: implications for fault growth, structure and permeability. *Journal of Structural Geology* **25**, 1779–94. doi: 10.1016/S0191-8141(03)00037-3.

Bouatia M, Demagh R and Derriche Z (2020) Structural behavior of pipelines buried in expansive soils under rainfall infiltration (Part I: transverse behavior). *Civil Engineering Journal* **6**, 1822–38. doi: 10.28991/cej-2020-03091585.

Brown ET and Hoek E (1978) Technical note: trends in relationships between measured in-situ stress and depth[J]. *International Journal of Rock Mechanics and Mining Sciences & Geomechanics Abstracts* **15**, 211–15. doi: 10.1016/0148-9062(78)91553-x.

Candela S, Mazzoli S, Megna A and Santini S (2015) Finite element modelling of stress field perturbations and interseismic crustal deformation in the Val d'Agri region, southern Apennines, Italy. *Tectonophysics* **657**, 245–59. doi: 10.1016/j.tecto.2015.07.011.

Cui X and Radwan A (2022) Coupling relationship between current in-situ stress and natural fractures of continental tight sandstone oil reservoirs. *Interpretation* **10**, 1–53. doi: 10.1190/int-2021-0200.1.

Deng S, Li H, Zhang Z, Wu X and Zhang J (2018) Characteristics of differential activities in major strike-slip fault zones and their control on hydrocarbon enrichment in Shunbei area and its surroundings, Tarim Basin. *Oil and Gas Geology* **39**, 38–48 (in Chinese with English abstract).

Deng S, Li H, Zhang Z, Zhang J and Yang X (2019) Structural characterization of intracratonic strike-slip faults in the central Tarim Basin. *AAPG Bulletin* **103**, 109–37. doi: 10.1306/06071817354.

Djurhuus J and Aadnoy BS (2003) In situ stress state from inversion of fracturing data from oil wells and borehole image logs. *Journal of Petroleum Science and Engineering* **38**, 121–30. doi: 10.1016/S0920-4105(03)00026-3.

Engelder T, Lash GG and Uzcategui RS (2009) Joint sets that enhance production from Middle and Upper Devonian gas shales of the Appalachian Basin. *AAPG Bulletin* **93**, 857–89. doi: 10.1306/03230908032.

Gale J, Reed RM and Holder J (2007) Natural fractures in the Barnett Shale and their importance for hydraulic fracture treatments. *AAPG Bulletin* **91**, 603–22. doi: 10.1306/11010606061.

Gao F (2021) Influence of hydraulic fracturing of strong roof on mining-induced stress: insight from numerical simulation. *Journal of Mining and Strata Control Engineering* **3**, 023032. doi: 10.13532/j.jmsce.cn10-1638/td.20210329.001.

Griffith W, Becker J, Cione K, Miller T and Pan E (2014) 3D topographic stress perturbations and implications for ground control in underground coal mines. *International Journal of Rock Mechanics & Mining Sciences* **70**, 59–68. doi: 10.1016/j.ijrmms.2014.03.013.

Hampel A and Hetzel R (2015) Horizontal surface velocity and strain patterns near thrust and normal faults during the earthquake cycle: the importance of viscoelastic relaxation in the lower crust and implications for interpreting geodetic data. *Tectonics* **34**, 731–52. doi: 10.1002/2014TC003605.

Han X, Deng S, Tang L and Cao Z (2017) Geometry, kinematics and displacement characteristics of strike-slip faults in the northern slope of Tazhong uplift in Tarim Basin: a study based on 3D seismic data. *Marine and Petroleum Geology* **88**, 410–27. doi: 10.1016/j.marpetgeo.2017.08.033.

Heidbach O, Rajabi M, Ziegler M, Reiter K and the WSM Team (2016) *The World Stress Map Database Release: Global Crustal Stress Pattern vs. Absolute Plate Motion*. Potsdam, Germany: European Geophysical Union General Assembly.

Hopkins CW (1997) The importance of in-situ-stress profiles in hydraulic-fracturing applications. *Journal of Petroleum Technology* **49**, 944–8. doi: 10.2118/38458-MS.

Husodon JA and Cooling CM (1988) In situ rock stresses and their measurement in U.K. – Part I. The current state of knowledge. *International Journal of Rock Mechanics and Mining Sciences and Geomechanics Abstracts* **25**, 363–70. doi: 10.1016/0148-9062(88)90976-X.

Jiao F (2017) Significance of oil and gas exploration in NE strike-slip fault belts in Shuntuoguole area of Tarim Basin. *Oil and Gas Geology* **38**, 831–9 (in Chinese with English abstract).

Jiao F (2018) Significance and prospect of ultra-deep carbonate fault-karst reservoirs in Shunbei area, Tarim Basin. *Oil and Gas Geology* **39**, 207–16 (in Chinese with English abstract).

Kaiser J (1950) *A study of acoustic phenomena in tensile tests*. PhD thesis, Technische Hochschule München, Munich, Germany. Published thesis.

Kanagawa T, Hayashi M and Nakasa H (1977) Estimation of spatial geostress components in rock samples using the Kaiser effect of acoustic emission. Proceedings of the Japan Society of Civil Engineers 1977, 63–75. doi: 10.2208/jscej1969.1977.258_63.

Khodaverdian A, Zafarani H and Rahimian M (2015) Long term fault slip rates, distributed deformation rates and forecast of seismicity in the Iranian Plateau. *Tectonics* **34**, 2190–20. doi: 10.1002/2014TC003796.

Lan S, Song D, Li Z and Liu Y (2021) Experimental study on acoustic emission characteristics of fault slip process based on damage factor. *Journal of Mining and Strata Control Engineering* **3**, 033024. doi: 10.13532/j.jmsce.cn10-1638/td.20210510.002.

Lee H, Olson J and Schultz R (2018) Interaction analysis of propagating opening mode fractures with veins using the discrete element method. *International Journal of Rock Mechanics and Mining Sciences* **103**, 275–88. doi: 10.1016/J.IJRMMS.2018.01.005.

Lu X, Wang Y, Tian F, Li X, Yang D, Li T, Lv Y and He X (2017) New insights into the carbonate karstic fault system and reservoir formation in the Southern Tahe area of the Tarim Basin. *Marine and Petroleum Geology* **86**, 587–605. doi: 10.1016/j.marpetgeo.2017.06.023.

Maerten L, Legrand X, Castagnac C, Lefranc M, Joonnekindt J-P and Maerten F (2019) Fault-related fracture modeling in the complex tectonic environment of the Malay Basin, offshore Malaysia: an integrated 4D geomechanical approach. *Marine and Petroleum Geology* **105**, 222–37. doi: 10.1016/j.marpetgeo.2019.04.025.

Marques FO, Ranalli G and Mandal N (2018) Tectonic overpressure at shallow depth in the lithosphere: the effects of boundary conditions. *Tectonophysics* **746**, 702–15. doi: 10.1016/j.tecto.2018.03.022.

Matsukik K, Nakama S and Sato T (2009) Estimation of regional stress by FEM for a heterogeneous rock mass with a large fault. *International Journal of Rock Mechanics and Mining Sciences* **46**, 31–50. doi: 10.1016/j.ijrmms.2008.03.005.

Mcclay K and Bonora M (2001) Analog models of restraining stepovers in strike-slip fault systems. *American Association of Petroleum Geologists Bulletin* **85**, 233–60. doi: 10.1016/S0378-7753(00)00605-4.

Mousavipour F, Riahi MA and Moghanloo HG (2020) Prediction of in situ stresses, mud window and overpressure zone using well logs in South Pars field. *Journal of Petroleum Exploration and Production Technology* **10**, 3–4. doi: 10.1007/s13202-020-00890-9.

Nelson EJ, Meyer JJ, Hillis RR and Mildren SD (2005) Transverse drilling-induced tensile fractures in the West Tuna area, Gippsland basin, Australia: implications for the in situ stress regime. *International Journal of Rock Mechanics & Mining Sciences* **42**, 361–71. doi: 10.1016/j.ijrmms.2004.12.001.

Nenna F and Aydin A (2011) The role of pressure solution seam and joint assemblages in the formation of strike-slip and thrust faults in a compressive tectonic setting; the Variscan of south-western Ireland. *Journal of Structural Geology* **33**, 1595–610. doi: 10.1016/j.jsg.2011.09.003.

Pollard D and Segall P (1987) Theoretical displacements and stresses near fractures in rock: with applications to faults, joints, veins, dikes, and solution surfaces. *Fracture Mechanics of Rock* **13**, 277–349. doi: 10.1016/B978-0-12-066266-1.50013-2.

Qi L (2016) Oil and gas breakthrough in ultra-deep Ordovician carbonate formations in Shuntuoguole uplift, Tarim Basin. *China Petroleum Exploration* **21**, 38–51 (in Chinese with English abstract).

Qu P, Shen R, Fu L, Zhang X and Yang H (2011) Application of the 3D discrete element method in the wellbore stability of coal-bed horizontal wells. *Acta Petrolei Sinica* **32**, 153–7 (in Chinese with English abstract).

Radwan A, Abdelghany W and Elkhawaga M (2021) Present-day in-situ stresses in Southern Gulf of Suez, Egypt: insights for stress rotation in an extensional rift Basin. *Journal of Structural Geology* **147**, 104334. doi: 10.1016/j.jsg.2021.104334.

Radwan A and Sen S (2021a) Stress path analysis for characterization of in situ stress state and effect of reservoir depletion on present-day stress magnitudes: reservoir geomechanical modeling in the Gulf of Suez Rift Basin, Egypt. *Natural Resources Research* **30**, 463–78. doi: 10.1007/s11053-020-09731-2.

Radwan A and Sen S (2021b) Characterization of in-situ stresses and its implications for production and reservoir stability in the depleted El Morgan hydrocarbon field, Gulf of Suez Rift Basin, Egypt. *Journal of Structural Geology*, 104355. doi: 10.1016/j.jsg.2021.104355.

Schultz R (2000) Growth of geologic fractures into large-strain populations: review of nomenclature, subcritical crack growth, and some implications for rock engineering. *International Journal of Rock Mechanics and Mining Sciences* **37**, 403–11. doi: 10.1016/S1365-1609(99)00115-X.

Song D, Li M and Wang TG (2013) Geochemical studies of the Silurian oil reservoir in the Well Shun-9 prospect area, Tarim basin, NW China. *Petroleum Science* **10**, 432–41. doi: 10.1007/s12182-013-0293-2.

Stephansson O and Zang A (2012) ISRM suggested methods for rock stress estimation – part 5: establishing a model for the in-situ stress at a given site. *Rock Mechanics and Rock Engineering* **45**, 955–69. doi: 10.1007/s00603-012-0270-x.

Sun S, Hou G and Zheng C (2019) Prediction of tensile fractures in KS2 trap, Kuqa Depression, NW China. *Marine and Petroleum Geology* **101**, 108–16. doi: 10.1016/j.marpetgeo.2018.11.037.

Tang L, Huang T, Qiu H, Qi L, Yang Y, Xie D, Yu Y, Zhao Z and Chen S (2012) Saltrelated structure and deformation mechanism of the Middle-Lower Cambrian in the middle-west parts of the Central Uplift and adjacent areas of the Tarim Basin. Science China Earth *Science* **55**, 1123–1133. doi: 10.1007/s11430-012-4414-3.

Wang Z, Gao Z, Fan T, Shang Y, Qi L and Yun L (2020) Structural characterization and hydrocarbon prediction for the SB5M strike-slip fault zone in the Shuntuo Low Uplift, Tarim Basin. *Marine and Petroleum Geology* **117**, 104418. doi: 10.1016/j.marpetgeo.2020.104418.

Woodcock NH and Rickards B (2003) Transpressive duplex and flower structure: Dent Fault System, NW England. *Journal of Structural Geology* **25**, 1981–92. doi: 10.1016/S0191-8141(03)00057-9.

Xie R, Zhou W, Liu C, Yin S, Radwan AE, Lei W and Cai W (2022) Experimental investigation on dynamic and static rock mechanical behavior, failure modes and sequences of frequent interbedded sand and shale reservoirs. *Interpretation* **10**, 1–52. doi: 10.1190/int-2021-0238.1.

Yin S, Ding W, Zhou W, Shan Y, Xie R, Guo C, Cao X, Wang R and Wang X (2017) In situ stress field evaluation of deep marine tight sandstone oil reservoir: a case study of Silurian strata in northern Tazhong area, Tarim Basin, NW China. *Marine and Petroleum Geology* **80**, 49–69. doi: 10.1016/j.marpetgeo.2016.11.021.

Yu J, Li Z and Yang L (2016) Fault system impact on paleokarst distribution in the Ordovician Yingshan Formation in the central Tarim basin, Northwest China. *Marine and Petroleum Geology* **71**, 105–18. doi: 10.1016/j.marpetgeo.2015.12.016.

Zeng L, Qi J and Wang Y (2007) Origin type of tectonic fractures and geological conditions in low-permeability reservoirs. *Acta Petrolei Sinica* **28**, 52–6 (in Chinese with English abstract).

Zhang J, Zhang Z, Wang B and Deng S (2018) Development pattern and prediction of induced fractures from strike-slip faults in Shunnan area, Tarim Basin. *Oil and Gas Geology* **39**, 955–63+1055 (in Chinese with English abstract).

Zhao K, Jiang P, Feng Y, Sun XD, Cheng LX and Zheng JW (2021) Investigation of the characteristics of hydraulic fracture initiation by using maximum tangential stress criterion. *Journal of Mining and Strata Control Engineering* **3**, 023520. doi: 10.13532/j.jmsce.cn10-1638/td.20201217.001.

Zhao R, Zhao T, Kong Q, Deng S and Li H (2020) Relationship between fractures, stress, strike-slip fault and reservoir productivity, China Shunbei oil field, Tarim Basin. *Carbonates and Evaporites* **35**. doi: 10.1007/s13146-020-00612-6.

Zhao R, Zhao T, Li H, Deng S and Zhang J (2019) Fault-controlled fracture-cavity reservoir characterization and main controlling factors in the Shunbei hydrocarbon field of Tarim Basin. *Special Oil & Gas Reservoirs* **26**, 8–13 (in Chinese).

Zhao T, Hu W, Zhao R, Yang M, Wang Q, Lin H, Ru Z, Bao D and Cao F (2021) Present in-situ stress distribution characteristics of strike-slip in SH Oilfield, Tarim Basin. *Arabian Journal of Geosciences* **14**, 1223. doi: 10.1007/s12517-021-07552-y.

Zhong J, Xu S, Chen Z and Ji S (2010) Analysis of fracture propagation path in anisotropic rock based on boundary element method. *Chinese Journal of Rock Mechanics and Engineering* **29**, 34–42 (in Chinese with English abstract).

Zhou C, Yin J, Luo J and Xiao GQ (2012) Law of geo-stress distribution in the vicinity of fault zone. *Journal of Yangze River Scientific Research Institute* **29**, 57–61 (in Chinese with English abstract).

Zhu Z and Song H (1990) *Structural Geology*. Wuhan: China University of Geosciences Press (in Chinese).

Zoback MD (2007) *Reservoir Geomechanics*. Cambridge: Cambridge University Press, 449 pp.

Zoback MD, Barton CA, Brudy M, Castillo DA, Finkbeiner T, Grollimund BR, Moos DB, Peska P, Ward CD, and Wiprut DJ (2003) Determination of stress orientation and magnitude in deep wells. *International Journal of Rock Mechanics & Mining Sciences* **40**, 1049–76. doi: 10.1016/j.ijrmms.2003.07.001.